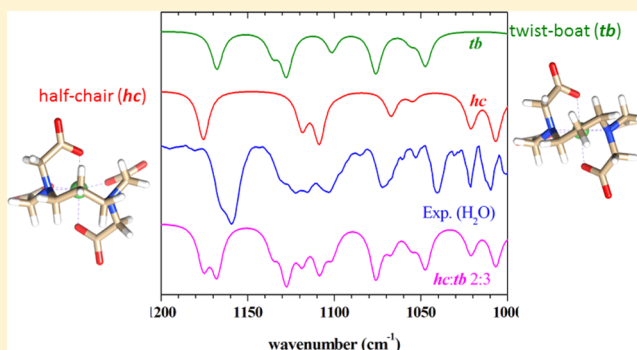


Secrets of Solid State and Aqueous Solution Structures of  $[\text{Ni}(\text{tmdta})]^{2-}$ Roland Meier,<sup>\*,†</sup> Carlos Platas-Iglesias,<sup>\*,‡</sup> Frank W. Heinemann,<sup>†</sup> Gerald Linti,<sup>§</sup> Jürgen Schulte,<sup>||</sup> and Sunil K. Srivastava<sup>⊥</sup><sup>†</sup>Inorganic Chemistry, Department of Chemistry and Pharmacy, Friedrich-Alexander-Universität Erlangen-Nürnberg, Egerlandstrasse 1, 91058 Erlangen, Germany<sup>‡</sup>Departamento de Química Fundamental, Universidade da Coruña, Campus da Zapateira, Rúa da Fraga 10, 15008, Coruña, Spain<sup>§</sup>Anorganisch-Chemisches Institut, University of Heidelberg, Im Neuenheimer Feld 270, D-69120 Heidelberg, Germany<sup>||</sup>Chemistry Department, Binghamton University, State University of New York, P.O. Box 6000 Binghamton, New York 13902-6000, United States<sup>⊥</sup>Department of Pure and Applied Physics, Guru Ghasidas Vishwavidyalaya, Koni, Bilaspur Chhattisgarh 495009, India

## S Supporting Information

**ABSTRACT:** The molecular structures of  $\text{Li}_2[\text{Ni}(\text{tmdta})] \cdot 5\text{H}_2\text{O}$  (**1a**, tmdta = trimethylenediaminetetraacetate),  $\{\text{C}(\text{NH}_2)_3\}_2[\text{Ni}(\text{tmdta})] \cdot 6\text{H}_2\text{O}$  (**1b**), and  $\{\text{Ni}(\text{H}_2\text{O})_6\}[\text{Ni}(\text{tmdta})] \cdot 2\text{H}_2\text{O}$  (**2a**) have been determined. The central trimethylenediamine chelate ring shows half-chair (*hc*) geometries in **1a** and **1b**, while a twist-boat (*tb*) conformation is encountered in **2a**. The coexistence of *tb* and *hc* forms in the solid state prompted us to elucidate the existence of a  $tb \rightleftharpoons hc$  equilibrium in aqueous solution. Evaluation of the data from solid state vibrational spectra (Raman and IR) for the *hc* and *tb* forms showed excellent agreement with simulated spectra obtained with DFT computations (TPSSH/TZVP). This outstanding matching between theory and experiment enabled

us to build composite spectra with varying *hc:tb* ratios. Comparison of these results with Raman and IR spectra recorded for  $[\text{Ni}(\text{tmdta})]^{2-}$  in aqueous solution revealed that simulated Raman and IR spectra with a *hc:tb* ratio = 2:3 match the solution spectra in an accurate way. This equilibrium ratio enabled us to compute  $^{13}\text{C}$  NMR shifts for the paramagnetic solution spectrum of  $[\text{Ni}(\text{tmdta})]^{2-}$  based on the relative contributions by *hc* and *tb* fractions. This leads to computed shifts that agree closely with the experimental ones. Also, the kinetics of the skeleton dynamics could be estimated quantitatively by temperature-dependent  $^{13}\text{C}$  NMR spectroscopic measurements. An interesting effect encountered for the very first time here concerns a drastic intensity difference of the  $10Dq$  band ( ${}^3\text{A}_2 \rightarrow {}^3\text{T}_2(\text{F})$  transition) in solid state electronic spectra of *tb* vs *hc* isomers, where the intensity of this band in the case of the *hc* form is much lower than that of the *tb* conformer and thus more similar to the case of the usual  $\text{Ni}^{\text{II}}$  chromophore in octahedral environment. The equilibrium constants for complex formation and protonation of  $\text{Ni}^{\text{II}}\text{-tmdta}$  at low pH have been estimated by pH-dependent UV-vis titration experiments. Correlation of these data with those of  $\text{Ni}^{\text{II}}\text{-edta}$  and related  $3d \text{M}^{\text{II}}$  edta and tmdta complexes allow important conclusions on the consequences resulting from extending the central diamine ring in the ligand by one methylene group in terms of both complex and protolytic stability for edta vs tmdta complexes.



## ■ INTRODUCTION

Polyaminocarboxylate ligands such as edta and related systems are efficient chelating agents used in laundry, textile, and paper industries to remove different metal ions. Edta is also used as an additive in food and beverages, cosmetics and personal care products, and cleansing agents. Furthermore, edta is utilized for chelation treatment of metal intoxication to treat poisoning with heavy metals such as lead.<sup>1,2</sup>

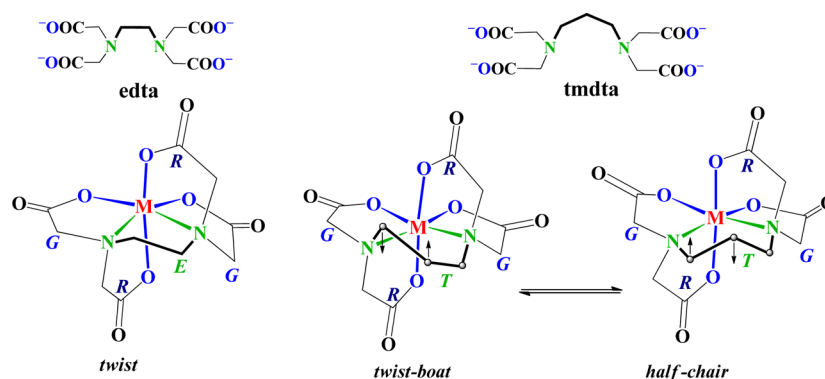
Replacement of the ethylene bridge in edta by a propylene spacer to give tmdta was shown to have significant effects on the structure and reactivity of the corresponding metal

complexes.<sup>3</sup> Complex formation with tmdta as compared to edta leads to formation of a six-membered instead of a five-membered chelate ring (see Scheme 1) in the central diamine branch of the corresponding complexes. While a regular symmetric gauche-type conformation of the diamine chelate ring (E ring) is usually found in six-coordinate edta complex structures, two different ring conformations are a priori possible in the diamine chelate ring (T ring) of a tmdta complex: Twist-

Received: February 25, 2014

Published: June 11, 2014

Scheme 1.  $tb \rightleftharpoons hc$  Equilibrium in Six-Coordinate tmdta Complexes Compared to the Twist Conformer of a Six-Coordinate edta Complex



boat (*tb*) and half-chair (*hc*) (cf. Scheme 1). The structure adopted by a particular complex in solution may have a dramatic impact on its properties. For instance, lanthanide complexes with the polyaminocarboxylate ligand dota (1,4,7,10-tetraazacyclododecane-1,4,7,10-tetraacetate) are known to exist in solution as two diastereoisomeric forms (**m** and **M**) that differ by the layout of their acetate arms.<sup>4</sup> However, it took almost 20 years after the first studies on these complexes<sup>5</sup> to discover that water exchange of the coordinated water molecule, a key parameter that controls their efficiency as MRI contrast agents, is about 2 orders of magnitude faster on the **m** isomer than on the **M** form.<sup>6</sup> The conformation adopted in solution by transition metal complexes was also found to play an important role in their efficiency catalyzing certain reactions (i.e., peptide hydrolysis<sup>7</sup>) or in their ability to bind biological substrates.<sup>8</sup> Thus, understanding the isomeric composition of a particular complex in solution and the factors that control it is of great importance to design chelates with the desired properties in a rational way. However, in the particular case of tmdta complexes the factors that govern the populations of *tb* and *hc* isomers remain largely unexplored, so that the approach presented here is an advent to clarify this query.

Inspection of the current version of the CCDC structural database (conquest 1.15, 2013) concerning adoption of *hc* or *tb* geometries in T rings of solid state tmdta complex structures reveals the following picture: One finds 34 independent structure estimations with 19 *tb* and 14 *hc* structures. The following structures with 3d  $M^{III}$  ions contain a pure T ring with *tb* conformations in six-coordinate complexes:  $K[Co(tmdta)] \cdot 2H_2O$ <sup>9</sup> and a related  $Co^{III}$  complex,<sup>10</sup> the series of isostructural sodium salts  $Na[M(tmdta)] \cdot 3H_2O$  with  $M = Cr^{III}$ ,  $Rh^{III}$ ,<sup>11</sup>  $Fe^{III}$ ,<sup>12</sup> and  $V^{III}$ ,<sup>13</sup> as well as  $K[Ga^{III}(tmdta)] \cdot 3H_2O$ .<sup>14</sup> Recently, structures of  $K[Fe(tmdta)]$ ,  $\{C(NH_2)_3\}[Fe(tmdta)] \cdot 3H_2O$ , and  $NH_4[Fe(tmdta)] \cdot 0.5H_2O$  were published containing also *tb* diamine fragments.<sup>15</sup>

Complex structures of tmdta with  $M^{II}$  ions and *tb* conformations in six-coordinate complexes were found in the isostructural series with the general formula  $\{M^a(H_2O)_6\} \cdot [M^b(tmdta)] \cdot 2H_2O$  where  $M^a = M^b$  in  $\{Co(H_2O)_6\} \cdot [Co(tmdta)] \cdot 2H_2O$ <sup>16</sup> and  $\{Zn(H_2O)_6\} \cdot [Zn(tmdta)] \cdot 2H_2O$ <sup>17</sup> as well as in  $\{Mg(H_2O)_6\} \cdot [Mg(tmdta)] \cdot 2H_2O$ .<sup>18</sup> In the other structures belonging to this series,  $M^a$  is Mg throughout and the structures are  $\{Mg(H_2O)_6\} \cdot [Ni(tmdta)] \cdot 2H_2O$ ,<sup>19</sup>  $\{Mg(H_2O)_6\} \cdot [Cu(tmdta)] \cdot 2H_2O$ ,<sup>20</sup>  $\{Mg(H_2O)_6\} \cdot [Co(tmdta)] \cdot 2H_2O$ ,<sup>16</sup>  $\{Mg(H_2O)_6\} \cdot [Zn(tmdta)] \cdot 2H_2O$ ,<sup>17</sup> as well as  $\{Mn(H_2O)_6\} \cdot [Cu(tmdta)] \cdot 2H_2O$ ,<sup>21</sup> where  $M^a = Mn$ . The salt  $\{Mg(H_2O)_6\} \cdot$

$[Mg_{0.5}Mn_{0.5}(tmdta)] \cdot 2H_2O$ <sup>22</sup> also with a *tb* T ring is an exception containing Mg and Mn equally distributed in the complex anion and can be regarded as a six-coordinate form of the  $Mn^{II}$ -tmdta system. However, compound  $\{Mg(H_2O)_6\} \cdot [Mn(tmdta)(H_2O)] \cdot 2H_2O$ <sup>22</sup> contains a seven-coordinate  $Mn^{II}$  center and a *hc*-configured T ring.

Complexes with coordination numbers (CNs) higher than 6 (7, 8, and 9) do not adopt the *tb* conformation, and the *hc* conformation is adopted throughout, which indicates that the latter fits much better to the geometric requirements of higher CNs. In addition to the complexes containing the  $Mn^{II}$ -OH<sub>2</sub> fragment,<sup>22</sup> there is another  $M^{II}$  complex showing CN 7 with  $Cd^{II}$  as the central ion with identical composition to its  $Mn^{II}$  relative, i.e.,  $\{Mg(H_2O)_6\} \cdot [Cd(tmdta)(H_2O)] \cdot 2H_2O$ .<sup>17,22</sup> The remaining  $M^{II}$ -tmdta complex contains an eight-coordinate  $Ca^{II}$  center in  $[Ca(H_2O)_3] \cdot [Ca(tmdta)(H_2O)] \cdot 2H_2O$ ,<sup>18</sup> which is the complex formula in the original paper. This structure contains a double  $\mu$ -aqua-bridged tmdta complex dimer  $[Ca(tmdta)(\mu-H_2O)]_2^{4-}$  with partially aquated calcium counter cations. The series of rare earth tmdta complex structures has been reported by Jun Wang and co-workers.<sup>23</sup> It is interesting that the whole series of CN 8  $Ln^{III}$ -tmdta complexes contains infinite chains of complex anions bridged by carboxylato groups with a  $\mu_2$ -carboxylato-*syn-anti* bridging mode, and the coordination sphere is completed by one coordinated water molecule.<sup>24</sup> There is one exception from this behavior found in the  $Yb^{III}$  monomer  $NH_4[Yb(tmdta)(H_2O)_2] \cdot 5H_2O$ .<sup>25</sup> Thus far, only one structure with an  $Ln^{III}$ -center exceeding CN 8 was found, the  $Sm^{III}$  dimer in  $K_2[\{Sm(\mu_2-tmdta)(H_2O)_2\}_2] \cdot 4.79H_2O$ ,<sup>26</sup> where the samarium centers are bound to two water molecules and are additionally doubly carboxylato bridged (bis( $\mu$ - $\eta^1$ -carboxylato)), giving rise to a 10-coordinated complex.

Not mentioned so far are the group of  $Li^+$  salts  $Li[Fe(tmdta)] \cdot 3H_2O$ <sup>15,27</sup> and  $Li_2[Co(tmdta)] \cdot 5H_2O$ .<sup>28</sup> The latter adopts a *hc* conformation, while  $Li[Fe(tmdta)] \cdot 3H_2O$  is essentially *hc* in the solid state. However, as outlined in a re-estimation of its structure,<sup>11</sup> a minor fraction of 8.7% *tb* does coexist in the presence of 91.3% *hc*. In the same way, the structure of  $\{C(NH_2)_3\}[Fe(tmdta)] \cdot 2H_2O$  is also peculiar, as 94% *tb* form is present with a minor fraction of 6% *hc*. The main goal of the present study is thus to elucidate the solution structure of the  $Ni^{II}$ -tmdta system, in particular addressing the possible presence of a  $tb \rightleftharpoons hc$  equilibrium in solution. Thus, we have chosen  $Li^+$  and  $\{C(NH_2)_3\}^+$  as counter cations for salt preparations with the aim to isolate *hc* isomers in the solid state.

This was planned because when our study was started only the crystal structure of  $\{\text{Mg}(\text{H}_2\text{O})_6\}[\text{Ni}(\text{tmdta})]\cdot 2\text{H}_2\text{O}$  (**2b**) was known in which the central diamine chelate ring adopts a *tb* conformation as described above. The strategy that we intended to adopt for our investigation is essentially identical to the approach applied in a previous work.<sup>15</sup> Solid and aqueous solution structures were studied by vibrational spectroscopy (IR and Raman), supported by calculated IR and Raman spectra using density functional theory (DFT). Furthermore, a <sup>13</sup>C NMR study combined with DFT calculations was used to explore the kinetics of the interconversions in the chelate rings accompanying the *tb*  $\rightleftharpoons$  *hc* equilibrium reactions. Finally, theoretical calculations of the contact <sup>13</sup>C NMR shifts were used to determine accurately the population of the *tb* and *hc* conformers in solution.

## EXPERIMENTAL AND COMPUTATIONAL SECTION

**Materials and Methods. Preparations.** Note that our approach to prepare  $[\text{Ni}(\text{tmdta})]^{2-}$  salts is completely different to that used by Radanovic et al.<sup>19</sup> to prepare the closely related  $[\text{Mg}(\text{H}_2\text{O})_6][\text{Ni}(\text{tmdta})]\cdot 2\text{H}_2\text{O}$  (**2b**) salt. Our approach avoided the use of column chromatography because the ligand was prepared directly in the form of the free acid  $\text{H}_4\text{tmdta}$ <sup>29</sup> or was used in that form from commercial sources (Sigma-Aldrich).

$\text{Li}_2[\text{Ni}(\text{tmdta})]\cdot 5\text{H}_2\text{O}$  (**1a**). A suspension of  $\text{H}_4\text{tmdta}$  (3.06 g, 0.01 mol) in 20 mL of water was heated with stirring to 70 °C. After addition of a first portion of  $\text{Li}_2\text{CO}_3$  (0.01 mol, 0.74 g), a clear solution resulted. Then 3.66 g (0.01 mol) of  $\text{Ni}(\text{ClO}_4)_2\cdot 6\text{H}_2\text{O}$  was added under stirring. A second portion of  $\text{Li}_2\text{CO}_3$  (0.01 mol, 0.74 g) was added (one has to be careful during both additions of  $\text{Li}_2\text{CO}_3$  because of the very intensive development of  $\text{CO}_2$ !), and heating was continued for 1 h. The resulting blue solution was placed in the refrigerator. After a period of several days, greenish-blue crystals were formed. These were collected by suction filtration and washed with cold water and ethanol. Recrystallization was carried out from a water–ethanol mixture. Yield: 3.7 g (80%). Anal. Calcd for  $\text{C}_{11}\text{H}_{34}\text{Li}_2\text{N}_2\text{NiO}_{13}$  (464.9): C, 33.58; H, 7.81; N, 6.03. Found: C, 33.50; H, 7.86; N, 6.00. Single crystals suitable for X-ray structure determination were prepared in the following way: A concentrated aqueous solution of **1** was gently layered with the 3-fold volume of ethanol in a large reagent glass. Crystals suitable for X-ray diffraction formed after several days. These were removed by hand picking.

$[\text{C}(\text{NH}_2)_3][\text{Ni}(\text{tmdta})]\cdot 6\text{H}_2\text{O}$  (**1b**). A suspension of  $\text{H}_4\text{tmdta}$  (3.06 g, 0.01 mol) in 30 mL of water was heated with stirring to 70 °C. A 2.9 g amount (0.01 mol) of  $[\text{Ni}(\text{H}_2\text{O})_6]\cdot 2\text{NO}_3$  was added to this solution, which gave in a short moment a turquoise blue solution. After stirring for further 10 min at 70 °C, the solution was cooled to room temperature. Then, a 3.6 g amount of  $[\text{C}(\text{NH}_2)_3]\text{CO}_3$  (0.02 mol) was gently added to the solution in portions, which resulted in a color change to clear deep blue. Standing of the clear solution at room temperature over 2 days led to the separation of clear, deep blue crystals, which were separated by filtration. Yield: 5.0 g (85%). Anal. Calcd for  $\text{C}_{13}\text{H}_{38}\text{NiN}_8\text{O}_{14}$  (589.2): C, 26.50; H, 6.50; N, 19.02. Found: C, 26.48; H, 6.63; N, 18.89. Single crystals suitable for X-ray structure determination were prepared in the following way: A concentrated aqueous solution of **1b** was set aside in a Petri dish. Crystals suitable for X-ray diffraction formed after 1 week.

$[\text{Ni}(\text{H}_2\text{O})_6][\text{Ni}(\text{tmdta})]\cdot 2\text{H}_2\text{O}$  (**2a**). This solid formed accidentally during a trial to prepare **1b** where only one-half of the amount of  $[\text{C}(\text{NH}_2)_3]\text{CO}_3$  was added. Therefore, the procedure to make **2a** is completely identical to that of **1b** except that 1.8 g (0.01 mol) of  $[\text{C}(\text{NH}_2)_3]\text{CO}_3$  was added to a solution containing  $\text{H}_4\text{tmdta}$  (3.06 g, 0.01 mol) and 2.9 g (0.01 mol) of  $[\text{Ni}(\text{H}_2\text{O})_6]\cdot 2\text{NO}_3$  in 30 mL of water. Crystals formed after 1 week of standing of this solution, had a regular shape, and were suitable for structural analysis. Yield: 4.5 g (80%). Anal. Calcd for  $\text{C}_{11}\text{H}_{30}\text{N}_2\text{Ni}_2\text{O}_{16}$  (563.8): C, 23.44; H, 5.36; N, 4.97. Found: C, 23.36; H, 5.42; N, 4.93.

$[\text{Mg}(\text{H}_2\text{O})_6][\text{Ni}(\text{tmdta})]\cdot 2\text{H}_2\text{O}$  (**2b**). A suspension of  $\text{H}_4\text{tmdta}$  (3.06 g, 0.01 mol) in 20 mL of water was heated with stirring to 70 °C. After addition of a first portion of  $\text{MgCO}_3\cdot 3\text{H}_2\text{O}$  (0.01 mol, 1.38 g), a clear solution resulted. Subsequently, 3.66 g (0.01 mol) of  $\text{Ni}(\text{ClO}_4)_2\cdot 6\text{H}_2\text{O}$  was added under stirring. A second portion of  $\text{MgCO}_3\cdot 3\text{H}_2\text{O}$  (0.01 mol, 1.38 g) was added. After carbon dioxide formation ceased, a deep blue solution resulted. This was layered with a solution of ethanol until the first turbidity appears and placed then in a refrigerator. A crystalline solid formed after 3 days, which was collected by vacuum filtration. Yield: 4.7 g (89%). Anal. Calcd for  $\text{C}_{11}\text{H}_{30}\text{MgN}_2\text{NiO}_{16}$  (529.4): C, 24.96; H, 5.71; N, 5.29. Found: C, 24.89; H, 5.77; N, 5.25.

**NMR Measurements.** A 930 mg amount of  $\text{Li}_2[\text{Ni}(\text{tmdta})]\cdot 5\text{H}_2\text{O}$  was dissolved in  $\text{D}_2\text{O}$  (1 mL, solution concentration 2 M) and filled into a 5 mm NMR tube. Variable-temperature 25.2 MHz <sup>13</sup>C NMR spectra were recorded on a Bruker AC 100 NMR spectrometer at 293, 333, 353, and 373 K. For each spectrum 100 000 scans were acquired using a 0.5 s recycle time with a spectral width of 1600 ppm and the transmitter frequency centered at  $-200$  ppm. The FIDs were treated with an exponential window function with 50 Hz line broadening prior to Fourier transformation. Resulting spectra were referenced against trimethylsilyl propionate (TSP) as an external standard.

**Estimation of Equilibrium Constants by pH-Dependent Spectrophotometric Measurements.** pH measurements were performed on a Metrohm 632 pH-meter equipped with a Mettler Toledo InLab 422 glass electrode, which was filled with NaCl instead of KCl to prevent precipitation of  $\text{KClO}_4$ . UV–vis spectra were recorded on a Cary 5G UV/vis/near-IR spectrophotometer.

**Vis/NIR Spectroscopy.** UV/vis/NIR spectra of the solid complexes were recorded on a PerkinElmer Lambda-900 instrument in reflection mode using a small spot praying mantis accessory belonging to the Lambda-900. Sample holders with varying surface areas were used. Baselines were recorded using a white standard sample holder (PTFE-coated).

**Raman Spectra.** Raman spectra of solid samples were recorded with a BRUKER IFS 66 device, while spectra of complexes in aqueous solutions were measured with a JOBIN YVON Ramanor HG 2S. In both cases, the 457.9 nm line of an argon laser was applied as an excitation source.

**Structure Determinations.** Crystal data and experimental details are compiled in Table S1 (Supporting Information). Suitable single crystals were sealed in glass capillaries. Intensity data were collected at 294(2) K on a Nicolet R3m/V four-circle diffractometer (Mo  $K\alpha$  radiation,  $\lambda = 0.71073$  Å, graphite monochromator,  $\omega$  scans) up to  $2\theta_{\text{max}} = 64^\circ$  or on a STOE IPDS I image-plate system at 200 K. A numeric absorption correction was applied for **1b** and **2a**. A semiempirical absorption correction using  $\psi$  scans was applied. Both structures were solved by direct methods and refined by full matrix least-squares procedures based on  $F^2$  with all unique reflections (SHELXTL NT 5.10).<sup>30</sup> All non-hydrogen atoms were refined anisotropically. All hydrogen atoms were located in a difference Fourier map and refined isotropically. Both the positional parameters and a common isotropic displacement parameter have been kept fixed during the refinement.

Crystallographic data (excluding structure factors) for the structures reported in this paper have been deposited with the Cambridge Crystallographic Data Center as supplementary publication nos. CCDC-977639 (**1a**), CCDC-977640 (**1b**), and CCDC-975639 (**2a**). Copies of the data can be obtained free of charge on application to CCDC, 12 Union Road, Cambridge CB2 1EZ, UK (fax: (+44)1223-336-033; e-mail: deposit@ccdc.cam.ac.uk).

**Theoretical and Computational Details.** All calculations presented in this work were performed employing the Gaussian 09 package (Revision A.01).<sup>31</sup> Full geometry optimizations of the  $[\text{Ni}(\text{tmdta})]^{2-}$  and  $[\text{Zn}(\text{tmdta})]^{2-}$  systems were performed in aqueous solution employing DFT within the hybrid meta-GGA approximation with the TPSSh exchange-correlation functional.<sup>32</sup> Input geometries were generated from the corresponding crystallographic data. In these calculations we used the standard Ahlrichs' valence triple- $\xi$  including polarization functions (TZVP).<sup>33</sup> No symmetry constraints have been imposed during the optimizations. In the case of  $\text{Ni}^{\text{II}}$  complexes the

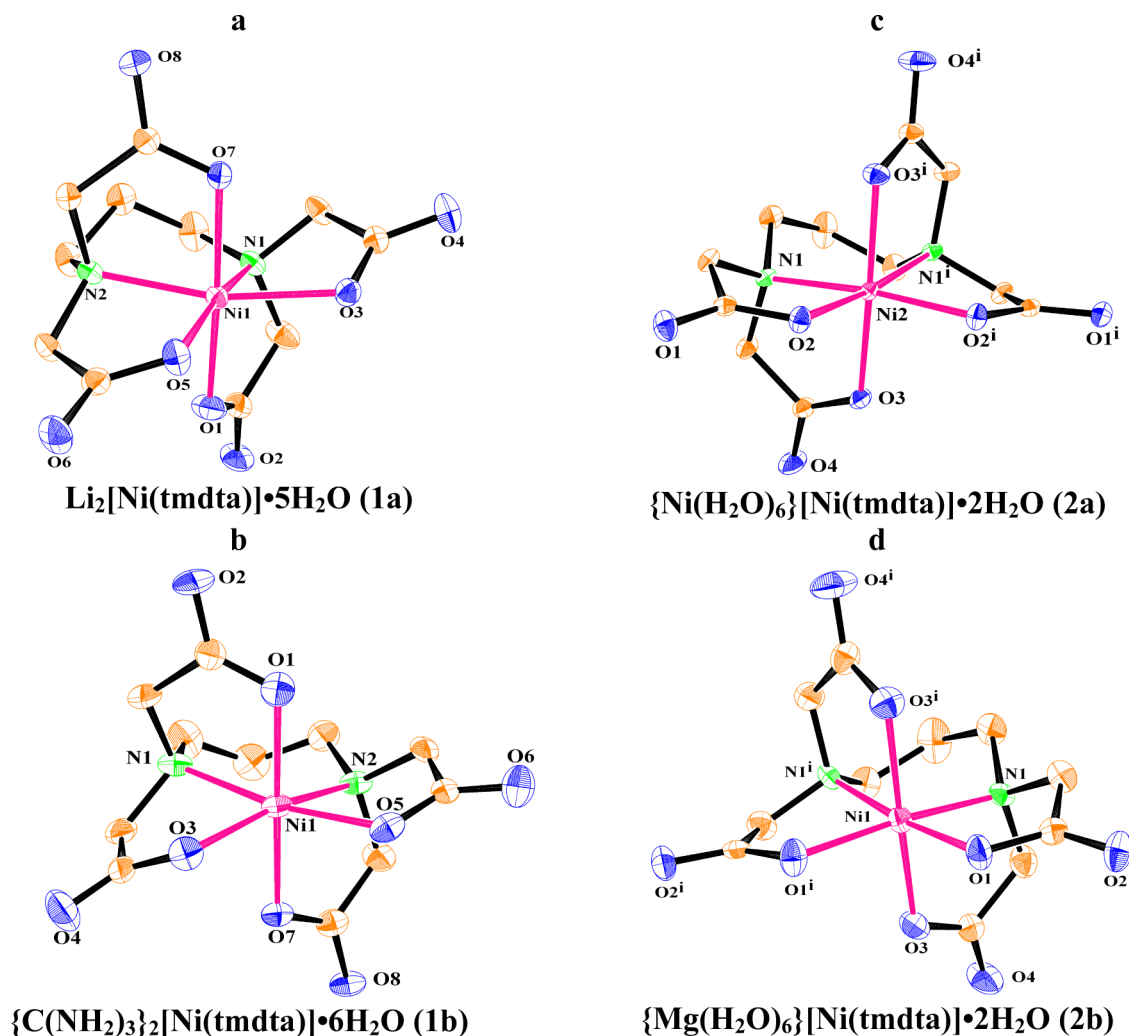


**Figure 1.** ORTEP drawings of  $[\text{Ni}(\text{tmdta})]^{2-}$  units in  $\text{Li}_2[\text{Ni}(\text{tmdta})] \cdot 5\text{H}_2\text{O}$  (1a),  $[\text{C}(\text{NH}_2)_3]_2[\text{Ni}(\text{tmdta})] \cdot 6\text{H}_2\text{O}$  (1b),  $\{\text{Ni}(\text{H}_2\text{O})_6\}[\text{Ni}(\text{tmdta})] \cdot 2\text{H}_2\text{O}$  (2a), and  $\{\text{Mg}(\text{H}_2\text{O})_6\}[\text{Ni}(\text{tmdta})] \cdot 2\text{H}_2\text{O}$  (2b).<sup>19</sup>

highest spin state was considered as the ground state (triplet). Since these calculations performed on the  $[\text{Ni}(\text{tmdta})]^{2-}$  complex used an unrestricted model, spin contamination<sup>34</sup> was assessed by a comparison of the expected difference between  $S(S+1)$  for the assigned spin state ( $S(S+1) = 2.0$  for the mononuclear  $\text{Ni}^{\text{II}}$  complexes investigated here) and the actual value of  $\langle S^2 \rangle$ .<sup>35</sup> The results obtained indicate that spin contamination is negligible for systems investigated in this work [ $\langle S^2 \rangle - S(S+1) \approx 0.0030$ ]. The stationary points found on potential energy surfaces as a result of geometry optimizations were tested to represent energy minima rather than saddle points via frequency analysis. Default values for the integration grid (75 radial shells and 302 angular points) and the SCF energy convergence criteria ( $10^{-8}$ ) were used in all calculations. The interconversions between the twist-boat (*tb*) and half-chair (*hc*) forms and the exchange between in-plane and out-of-plane glycinic rings of  $[\text{Ni}(\text{tmdta})]^{2-}$  were investigated by means of the synchronous transit-guided quasi-Newton method.<sup>36</sup> The nature of the saddle points (one imaginary frequency) was characterized by frequency analysis. The relative free energies of the two energy minima and the free energy barrier for their interconversion were calculated in aqueous solution at the TPSSh/TZVP level, and they include non-potential-energy contributions (zero-point energies and thermal terms) obtained through frequency analysis.

Isotropic  $^1\text{H}$  and  $^{13}\text{C}$  HFCCs of the *hc* and *tb* forms of  $[\text{Ni}(\text{tmdta})]^{2-}$  were calculated in aqueous solution with unrestricted DFT methods by employing the TPSSh functional and the TZVP basis set for Ni. In all DFT investigations of HFCCs specifically

developed basis sets with extra flexibility in the core region should be employed.<sup>37</sup> Thus, for the description of C, H, N, and O we used the EPR-III basis sets of Barone,<sup>38</sup> which is a triple- $\zeta$  basis set including diffuse functions, double d polarizations, and a single set of f-polarization functions, together with an improved s-part to better describe the nuclear region. The isotropic Fermi contact contribution ( $A_{\text{iso}}$ ) of the hyperfine coupling tensor for a nucleus  $N$  is given by<sup>39</sup>

$$A_{\text{iso}}(N) = \frac{4\pi}{3S} \mu_{\text{B}} \mu_{\text{N}} g_{\text{e}} g_{\text{N}} \rho^{\alpha-\beta}(R_{\text{N}}) \quad (1)$$

where  $\mu_{\text{B}}$  and  $\mu_{\text{e}}$  are the nuclear and Bohr magnetons, respectively,  $g_{\text{N}}$  and  $g_{\text{e}}$  are nuclear and free-electron  $g$  values,  $S$  is the total spin of the system, and  $\rho^{\alpha-\beta}$  represents the difference between majority spin ( $\alpha$ ) and minority spin ( $\beta$ ) densities.

The NMR shift observed for a given nucleus  $i$  of a paramagnetic metal ion  $j$  ( $\delta_{ij}^{\text{exp}}$ ) is the result of both paramagnetic ( $\delta_{ij}^{\text{para}}$ ) and diamagnetic ( $\delta_{ij}^{\text{dia}}$ ) contributions

$$\delta_{ij}^{\text{exp}} = \delta_{ij}^{\text{para}} + \delta_{ij}^{\text{dia}} \quad (2)$$

The paramagnetic contribution to the observed chemical shifts is the result of both contact and pseudocontact contributions. However,  $^{13}\text{C}$  NMR paramagnetic shifts of  $\text{Ni}^{2+}$  complexes are expected to be largely contact in origin, although nuclei residing far away from the paramagnetic center in terms of number of bonds might have sizable pseudocontact contributions. The contact contribution may be approximated by the following equation

Table 1. Comparison of Bond Distances and Angles of Structures 1a, 1b, and 2a with Those of 2b

parameter	1a ( <i>hc</i> )	1b ( <i>hc</i> )	2a ( <i>tb</i> )	2b ( <i>tb</i> )
Ni–N <sub>1</sub>	2.0935(19) Å	2.132(9) Å	2.0793(14) Å (N1)	2.073(5) Å (N1)
Ni–N <sub>2</sub>	2.0886(15) Å	2.087(9) Å	2.0793(14) Å (N1')	2.073(5) Å (N1')
(Ni–N) <sub>av</sub>	2.091(3) Å	2.11(3) Å	2.0793(14) Å	2.073(5) Å
Ni–O <sub>G1</sub>	2.1084(13) Å (O3)	2.091(7) Å (O3)	2.0241(12) Å (O2)	2.027(5) Å (O1)
Ni–O <sub>G2</sub>	2.0517(17) Å (O5)	2.098(7) Å (O5)	2.0241(12) Å (O2')	2.027(5) Å (O1')
(Ni–O <sub>G</sub> ) <sub>av</sub>	2.08(4) Å	2.095(5) Å	2.0241(12) Å	2.027(5) Å
Ni–O <sub>R1</sub>	2.0795(14) Å (O1)	2.076(1) Å (O1)	2.0763(12) Å (O3)	2.078(5) Å (O3)
Ni–O <sub>R2</sub>	2.0780(12) Å (O7)	2.075(7) Å (O7)	2.0763(12) Å (O3')	2.078(5) Å (O3')
(Ni–O <sub>R</sub> ) <sub>av</sub>	2.079(1) Å	2.076(8) Å	2.0763(12) Å	2.078(5) Å
$\alpha$	101.61(6)°	100.9(3)°	96.37(5)°	96.4(4)°
$\beta_1$	79.52(6)°	78.3(3)°	81.16(5)°	82.5(2)°
$\beta_2$	80.06(6)°	78.4(3)°	81.16(5)°	82.5(2)°
$\gamma$	101.40(5)°	104.5(3)°	98.07(5)°	99.4(2)°
$\beta_3$	81.12(6)°	81.9(3)°	82.45(5)°	82.47(19)°
$\beta_4$	81.66(5)°	83.1(3)°	82.45(5)°	82.47(19)°
$\delta$	175.07(6)°	178.1(3)°	175.30(5)°	175.1(2)°

$$\delta_{ij}^{\text{con}} = \frac{g_e \mu_B S(S+1) A}{3\gamma_I k_B T} \frac{A}{\hbar} \times 10^6 = \frac{F A}{\hbar} \quad (3)$$

where  $A/\hbar$  is the scalar hyperfine coupling constant,  $S$  is the total electron spin of the system,  $g_e$  is the free electron  $g$  value,  $\mu_B$  is the electron Bohr magneton,  $\gamma_I$  is the nuclear magnetogyric ratio, and  $T$  is the temperature.<sup>40</sup> In eq 3  $A/\hbar$  is expressed in  $\text{rad}\cdot\text{s}^{-1}$  and therefore equals  $2\pi A_{\text{iso}}$  as defined in eq 1.

The NMR shielding tensors of the  $[\text{Zn}(\text{tmdta})]^{2-}$  system were computed in aqueous solution at the TPSSh/TZVP level using the GIAO method.<sup>41</sup> For chemical shift calculation purposes, NMR shielding tensors of TMS were calculated at the same computational level. IR spectra were simulated from the calculated harmonic frequencies and IR intensities obtained through second derivatives, with the aid of the GaussView program.<sup>42</sup> A half width at half height of  $4\text{ cm}^{-1}$  was applied. Frequencies used to obtain the simulated spectra were unscaled. Raman spectra were simulated in a similar way from the harmonic frequencies and Raman intensities calculated from molecular polarizabilities. A half width at half height of  $8\text{ cm}^{-1}$  and a scaling factor of 1.05 were used.

Throughout this work solvent effects were included using the polarizable continuum model (PCM), in which the solute cavity is built as an envelope of spheres centered on atoms or atomic groups with appropriate radii. In particular, we used the integral equation formalism (IEFPCM) variant as implemented in Gaussian 09.<sup>43</sup>

## RESULTS AND DISCUSSION

**Structural Features of 1a, 1b, and 2a compared with 2b.** The structure of **1a** (cf. Figure 1a; for asymmetric unit cf. Figure S1a, Supporting Information) contains two crystallographically independent  $\text{Li}^+$  tetrahedra, a six-coordinate  $[\text{Ni}(\text{tmdta})]^{2-}$  complex anion, and five crystal water molecules, where three are Li bound and two are fixed only by H bonds. Basic crystallographic features for structures **1a** in comparison to **1b** and **2a** are collected in Table S1 (Supporting Information).

The  $\text{Ni}^{\text{II}}\text{N}_2\text{O}_4$  core comprises a severely distorted octahedron (similar to the one in structure **1b**, see below) when compared with those found in structures **2a** and **2b**. This becomes evident by comparison of the deviation of the four in-plane  $\text{L}-\text{Ni}-\text{L}'$  angles from the ideal value of  $90^\circ$ . The sums of the individual deviations are  $43.4^\circ$  (**1a**),  $48.7^\circ$  (**1b**),  $32.1^\circ$  (**2a**), and  $30.8^\circ$  (**2b**). This is a consequence of the different diamine chelate ring conformations: half-chair in **1a** and **1b** vs twist-boat in **2a** and **2b** (cf. Figure 1d). The peculiarity of the salt structure **1a** is

that crystallization takes place in the homochiral space group  $P2_1$ , which has already been observed for the isostructural salt  $\text{Li}_2[\text{Co}(\text{tmdta})]\cdot 5\text{H}_2\text{O}$ .<sup>28</sup> As described there, the main reason for chiral discrimination in the course of crystallization is the special type of rigidification of the chelate matrix by the peculiar lithium dimer encountered in both isostructural complex salts.

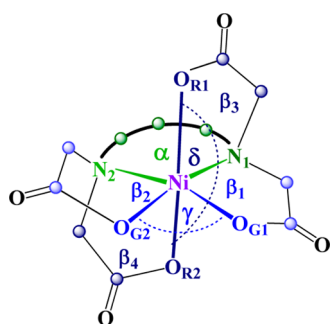
The structure of **1b** (cf. Figure 1b; for asymmetric unit cf. Figure S1b, Supporting Information) consists of two  $\{\text{C}(\text{NH}_2)_3\}^+$  cations, a  $[\text{Ni}(\text{tmdta})]^{2-}$  unit, and 6 water molecules of crystallization. As mentioned above, the deviation from octahedral symmetry is more pronounced in **1b**.

There are two octahedral  $\text{Ni}^{\text{II}}$  units ( $[\text{Ni}(\text{tmdta})]^{2-}$  and  $[\text{Ni}(\text{H}_2\text{O})_6]^{2+}$ ) and two waters of crystallization in the structure of **2a** (cf. Figure 1c; asymmetric unit cf. Figure S1c, Supporting Information). As required by crystallographic symmetry of the orthorhombic space group  $Pnna$ , a  $C_2$  axis (highest symmetry element in this structure) passes through the Ni2 center and the central carbon (C2) of the T ring. Atoms Ni2 and C2 of the T ring are on special positions 4d of space group  $Pnna$ . Thus, the complex has  $C_2$  symmetry. Both in-plane (G) glycinate rings are symmetry equivalent, as well as both out-of-plane (R) glycinate rings. The puckering extent of the glycinate rings is much more pronounced for G than for R rings, in line with the work of Hoard et al.,<sup>44</sup> who also introduced the G, R notation.

Important bond lengths and angles of the structures determined here (**1a**, **1b**, and **2a**) are compared with data of **2b**<sup>19</sup> in Table 1. The bond lengths and angles in Table 1 are assigned according to the donor atom pattern shown in Scheme 2. Both *hc* structures show Ni–N bond distances  $(\text{Ni}-\text{N})_{\text{av},hc} = 2.10(2)\text{ \AA}$ , somewhat longer than those found in the *tb* structures  $(\text{Ni}-\text{N})_{\text{av},tb} = 2.076(4)\text{ \AA}$ . This is a consequence of different degrees of strain depending upon if the  $\text{Ni}^{\text{II}}$  center is either wrapped by tmdta in the *hc* or the *tb* coordination mode. Clearly, Ni–N bonding is less strained in the *tb* structures.

The  $(\text{Ni}-\text{O}_G)_{\text{av}}$  distances in *hc* structures **1a** ( $2.08(4)\text{ \AA}$ ) and **1b** ( $2.095(5)\text{ \AA}$ ) are slightly longer than the corresponding  $(\text{Ni}-\text{O}_R)_{\text{av}}$  bonds ( $2.079(1)\text{ \AA}$  for **1a** and  $2.076(8)\text{ \AA}$  for **1b**). This is different in the case of *tb* structures **2a** and **2b** where the Ni–O<sub>G</sub> bond lengths are in both cases ( $\text{Ni}-\text{O}_G = 2.0241(12)\text{ \AA}$  for **2a** and  $2.027(5)\text{ \AA}$  for **2b**) significantly shorter than Ni–O<sub>R</sub> distances ( $\text{Ni}-\text{O}_R = 2.0763(12)\text{ \AA}$  for **2a** and  $2.078(5)\text{ \AA}$  for **2b**). The initial assumption that the longer Ni–O<sub>R</sub> distances are caused by packing effects had to be discarded because the *tb*

Scheme 2. Indication of Donor Atoms and Bond Angles Used in Current Work



structure obtained by DFT geometry optimization in aqueous solution (TPSSH/TZVP) shows the same pattern of (Ni–O<sub>G</sub>) vs (Ni–O<sub>R</sub>) bond length difference, i.e., the in-plane Ni–O<sub>G</sub> bond distances are substantially shorter than out-of-plane Ni–O<sub>R</sub> bonds. This is in contrast to the bond length patterns of *tb* M<sup>III</sup>–tmdta structures observed in the isostructural salts Na[M(tmdta)]·3H<sub>2</sub>O<sup>11–13</sup> including K[Co(tmdta)]·2H<sub>2</sub>O,<sup>9</sup> which are analyzed in Figure 2 using Shannon plots. In a Shannon plot, M–L distances from crystal structure analysis are related to hypothetical bond lengths constructed from the sum of the Shannon radii (Shannon radius = IR)<sup>45</sup> between the appropriate metal ion M and the ligand donor atom L ((M–

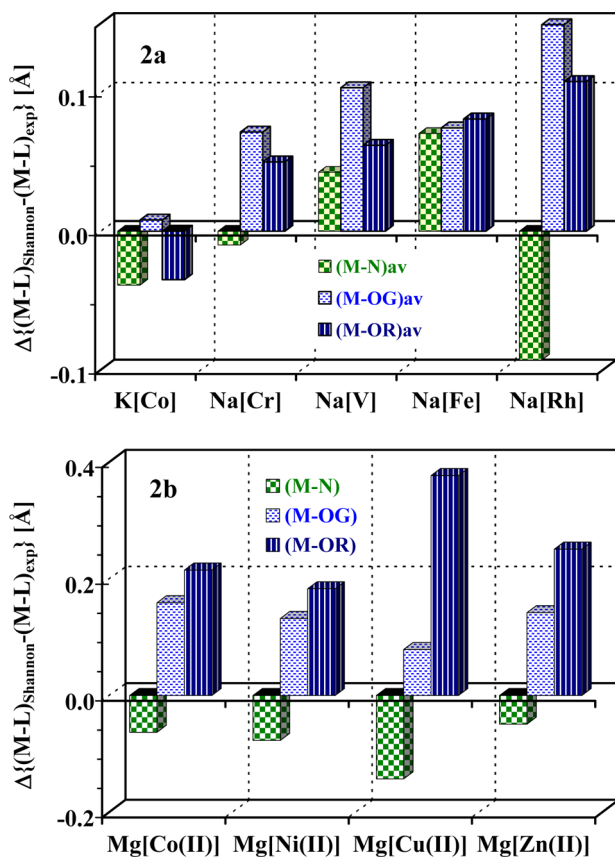


Figure 2. (a) Shannon plots of the M–L distances in the *tb* complex anions of salt structures Na[M<sup>III</sup>(tmdta)]·3H<sub>2</sub>O<sup>11–13</sup> and K[Co<sup>III</sup>(tmdta)]·2H<sub>2</sub>O. (b) Shannon plot of the M–L distances in the *tb* complex anions of salt structures {Mg(H<sub>2</sub>O)<sub>6</sub>}[M<sup>II</sup>(tmdta)]·2H<sub>2</sub>O.<sup>16,17,19,20</sup> Donor atom indication is as shown in Scheme 2.

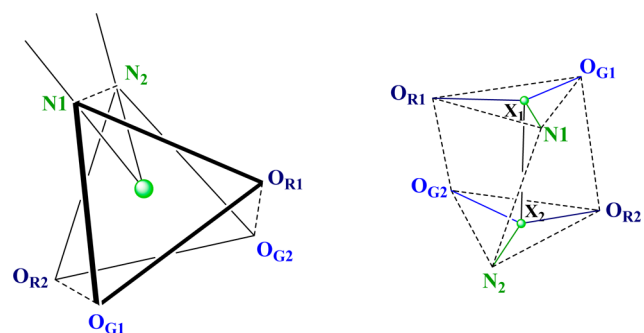
L)<sub>Shannon</sub> = IR(M<sup>n+</sup>) + IR(L)). Thus,  $\Delta = \{(M-L)_{\text{Shannon}} - (M-L)_{\text{exp}}\}$  values have a positive sign if (M–L)<sub>exp</sub> is shorter than (M–L)<sub>Shannon</sub>, while a negative sign results if (M–L)<sub>exp</sub> is longer than (M–L)<sub>Shannon</sub>.

As shown in Figure 2a, the M–O<sub>R</sub> distances are always shorter than M–O<sub>G</sub> for M = Co<sup>III</sup> (d<sup>6</sup> LS), Cr<sup>III</sup> (d<sup>3</sup>), V<sup>III</sup> (d<sup>2</sup>), and Rh<sup>III</sup> (d<sup>6</sup> LS) but the rule is broken in the case of Fe<sup>III</sup> (d<sup>5</sup> HS), where suddenly Fe–O<sub>R</sub> is somewhat longer than Fe–O<sub>G</sub>. There seems to be a simple explanation for this behavior: The main interaction responsible for binding of the carboxylate oxygen of tmdta is the result of a  $\sigma$  bonding due to donation of electron density from O p orbitals into the e<sub>g</sub> orbitals (d<sub>x<sup>2</sup>-y<sup>2</sup></sub>, d<sub>z<sup>2</sup></sub>) of the metal center. The e<sub>g</sub> sublevel is empty in the case of d<sup>6</sup> LS, d<sup>3</sup> HS, and d<sup>2</sup> HS configurations. In these cases, the better spatial overlap between the O p orbitals and the d<sub>z<sup>2</sup></sub> acceptor orbital at the metal site (along the z axis) leads to shorter M–O<sub>R</sub> and longer M–O<sub>G</sub> bonds.<sup>44</sup> As soon as the e<sub>g</sub> orbitals are filled with electrons as in the case of d<sup>5</sup> HS (Fe<sup>III</sup>), electrostatic repulsion between O p orbitals and d<sub>z<sup>2</sup></sub> acceptor orbitals leads to longer M–O<sub>R</sub> and shorter M–O<sub>G</sub> distances. The longer M–O<sub>G</sub> bonds are presumably also related to the weaker overlap between O p orbitals and d<sub>x<sup>2</sup>-y<sup>2</sup></sub> orbital on the metal site caused by the always greater puckering of G- vs R-glycinate rings.<sup>44</sup>

M–L bond length patterns in the {Mg(H<sub>2</sub>O)<sub>6</sub>}[M<sup>II</sup>(tmdta)]·2H<sub>2</sub>O *tb* structures with M = Co (d<sup>7</sup> HS),<sup>16</sup> Ni (d<sup>8</sup> HS),<sup>19</sup> Cu (d<sup>9</sup>),<sup>20</sup> and Zn (d<sup>10</sup>)<sup>17</sup> are compared in Figure 2b. Understanding of these patterns can be reached in a similar way as shown above for the M<sup>III</sup> structures. All these metal ions have partially (Co<sup>II</sup>, Ni<sup>II</sup>, Cu<sup>II</sup>) or fully (Zn<sup>II</sup>) occupied e<sub>g</sub> orbitals; thus, the greater electrostatic repulsion along the z axis leads to longer M–O<sub>R</sub> and shorter M–O<sub>G</sub> bonds as shown in Figure 2b.

As described above, there is no substantial difference between the Ni–O<sub>G</sub> and the Ni–O<sub>R</sub> distances in the case of the both *hc* structures 1a and 1b. However, there are important differences between *hc* structures 1a and 1b and *tb* structures 2a and 2b in terms of their deviation from regular O<sub>h</sub> symmetry. It has already been mentioned above that the in-plane L–Ni–L' angles are much more away from the ideal value of 90° for the *hc* form as compared to the *tb* one. Another measure of deviation from the regular octahedral symmetry is delivered by trigonal twist angles  $\phi$ ,<sup>46</sup> where  $\phi = 60^\circ$  for an ideal octahedron and  $\phi = 0^\circ$  for an ideal trigonal prism. The definition of the three  $\phi$  angles we used to obtain information concerning the deviation from strictly octahedral symmetry of the *cis*-NiN<sub>2</sub>O<sub>4</sub> cores of *tb* and *hc* salts of [Ni(tmdta)]<sup>2-</sup> is shown in Scheme 3. X<sub>1</sub> and X<sub>2</sub> are the centroids (geometric centers) of the triangles confined by N<sub>1</sub>, O<sub>G1</sub>, O<sub>R1</sub> and N<sub>2</sub>, O<sub>G2</sub>, O<sub>R2</sub>. The  $\phi_1$ ,  $\phi_2$ , and  $\phi_3$  values for structures 1a, 1b, 2a, and 2b are collected in Table 2. These data show unambiguously that there is some influence leading to irregular distortion in the *hc* structures away from O<sub>h</sub> symmetry, while both *tb* structures show a lesser degree of distortion. Also, the distortion is more pronounced in the case of the structure 1b relative to 1a. A detailed analysis of the structural data (see Supporting Information) shows that Dunitz plots are a convenient and an effective tool to judge puckering in five-membered and six-membered chelate ring.<sup>47</sup> These plots are based on the empirical finding by J. D. Dunitz that in five- and six-membered rings a linear relationship exists between the sum of the 5 intraring valence angles  $\sum \omega_{\text{ring}}$  and the squared sum of the 5 intraring torsion angles  $\sum \tau_{\text{ring}}^2$ .<sup>48</sup> The linear regression line through data in Figure 3 reveals the correctness of the data

Scheme 3. Location of Twist Angles  $\phi_1$ ,  $\phi_2$ , and  $\phi_3$  in the *cis*-NiN<sub>2</sub>O<sub>4</sub> Coordination Polyhedra<sup>a</sup>



$$^a \phi_1 = \tau_1 = \angle N_1 X_1 - X_2 N_2, \phi_2 = \tau_2 = \angle O_{G1} X_1 - X_2 O_{R2}, \phi_3 = \tau_3 = \angle O_{R1} X_1 - X_2 O_{G2}$$

Table 2. Trigonal Twist Angles  $\phi_1$ ,  $\phi_2$ , and  $\phi_3$  in structures 1a, 1b, 2a, and 2b

structure	1a ( <i>hc</i> )	1b ( <i>hc</i> )	2a ( <i>tb</i> )	2b ( <i>tb</i> )
$\phi_1$ (deg)	55.40	55.07	57.88	58.05
$\phi_2$ (deg)	52.56	50.59	57.30	57.30
$\phi_3$ (deg)	55.51	52.70	57.30	57.30

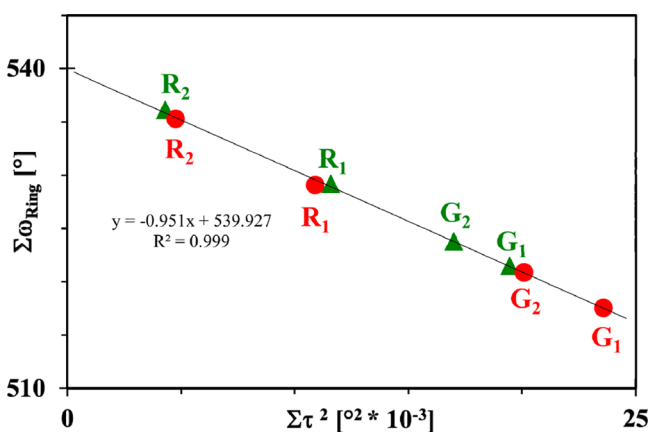


Figure 3. Dunitz plot reflecting the degree of puckering in the glycinate chelate rings of 1a (green triangles) and the DFT-optimized geometry obtained for the *hc* isomer (red circles). Agreement between theory and experiment is excellent. G rings in the DFT structure are somewhat more puckered than in 1a because the Ni–O–C angles in 1a are more acute by  $\sim 2^\circ$ .

because if  $\Sigma \omega_{\text{ring}} \approx \Sigma \tau_{\text{ring}}^2$  is strictly valid the plot should intersect the ordinate at  $\Sigma \omega_{\text{ring}} = 540^\circ$ , the value for the completely planar ring. The plot also shows that the chelate ring R<sub>1</sub> is considerably more puckered than R<sub>2</sub>. The puckering patterns of the glycinate chelate rings in the *tb* structures are more even than that shown in Figure 3 (cf. Figure S6, Supporting Information) and resemble the patterns found in R and G rings of [Ni(edta)]<sup>2-</sup> structures with rather flat R rings and G rings that are less puckered than those in the *hc* structures. A check of the structural distortions in the related tmdta complex structures Li[Fe(tmdta)]·3H<sub>2</sub>O and Li<sub>2</sub>[Co(tmdta)]·5H<sub>2</sub>O<sup>28</sup> reveals puckering patterns roughly identical to that found in 1a. A detailed analysis of the solid state and DFT geometries shows that intramolecular H···H repulsion between the various CH<sub>2</sub> groups are the main cause for the more important puckering of the glycinate chelate rings in the

*hc* structures, which in turn results in a more pronounced distortion of the coordination environment with respect to the regular octahedral coordination (see Supporting Information for details).

**Solution Structure and Dynamics.** <sup>13</sup>C NMR spectra of [Ni(tmdta)]<sup>2-</sup> (Figure 4) were recorded in D<sub>2</sub>O solution at

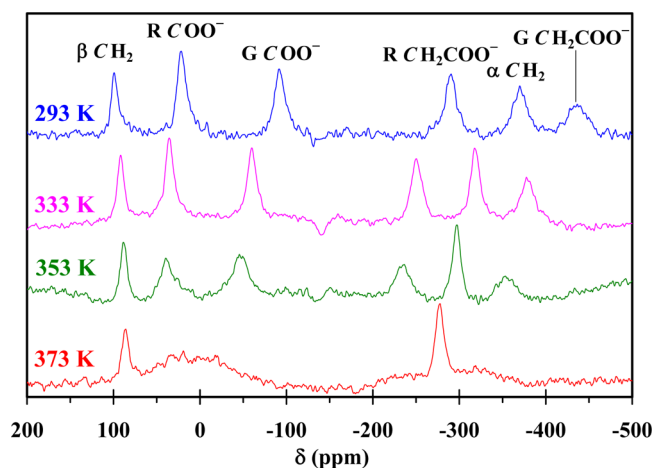


Figure 4. <sup>13</sup>C NMR spectra of [Ni(tmdta)]<sup>2-</sup> (25.2 MHz) recorded in D<sub>2</sub>O solution at different temperatures.

different temperatures. Spectra recorded in the temperature range 293–353 K show six resonances whose chemical shifts present a linear dependence with the reciprocal Kelvin temperature (Figure S8, Supporting Information), which indicates that the contact contribution dominates the Ni<sup>2+</sup>-induced paramagnetic shifts.<sup>49</sup> Assignment of the <sup>13</sup>C NMR signals (Table 4) was achieved by comparison with the shifts reported for [Ni(edta)]<sup>2-</sup> and [Ni(cytdta)]<sup>2-</sup><sup>50</sup> and confirmed by our DFT calculations described below. <sup>13</sup>C NMR signals due to the methylene carbon nuclei of the glycinate groups (R CH<sub>2</sub>COO<sup>-</sup> and G CH<sub>2</sub>COO<sup>-</sup>), observed at -281.5 and -424.7 ppm at 293 K, gradually broaden upon increasing temperature, and finally, they achieve coalescence at 373 K. A similar effect is observed for the two signals of the carbon nuclei of carbonyl groups, which are observed at 25.3 and -84.9 ppm at 293 K. This behavior reflects a dynamic exchange process that exchanges the positions of the out-of-plane (R) and in-plane (G) glycinate groups. From the chemical shift difference of the signals due to the methylene carbon nuclei and the coalescence temperature of 373 K we estimate an activation free energy for this dynamic process of 64.2 kJ mol<sup>-1</sup>, which corresponds to a rate  $k_c = 8.2 \times 10^3 \text{ s}^{-1}$  at this temperature. This rate is 2 orders of magnitude lower than that determined for the exchange of the coordinated water molecule in [Ni(tmdta)(H<sub>2</sub>O)]<sup>2-</sup>, which represents a very small fraction of the complex present in solution ( $f = 0.028$ ).<sup>3</sup> This implies that the two processes occur in completely different time scales, with many water exchange events taking place in between two interconversions of the R and G glycinate groups.

Aiming to obtain information on the structure in solution of the [Ni(tmdta)]<sup>2-</sup> complex we performed density functional theory (DFT) calculations at the TPSSh/TZVP level. In these calculations we have taken into account solvent effects (water) using a polarizable continuum model (PCM). Geometry optimizations provided two energy minima corresponding to the *tb* and *hc* forms of the complex. The agreement between the

DFT-optimized structures and those observed in the solid state is excellent (Table 3, see also Figures S9 and S11, Supporting Information).

**Table 3. Comparison of Bond Distances and Valence Angles of the Ni<sup>2+</sup> Centers in 1a and 2a with *hc* and *tb* Structures Optimized by DFT in Aqueous Solution (TPSSH/TZVP)**

	1a ( <i>hc</i> )	DFT <i>hc</i>	2a ( <i>tb</i> )	DFT <i>tb</i>
Ni–L distances (Angstroms)				
(Ni–N) <sub>av</sub>	2.091(3)	2.12(2)	2.08	2.11
(Ni–O <sub>G</sub> ) <sub>av</sub>	2.08(4)	2.078(1)	2.0241	2.062
(Ni–O <sub>R</sub> ) <sub>av</sub>	2.079(1)	2.080(1)	2.0763	2.073
L–Ni–L' angles (degrees)				
$\alpha$	101.61(6)	102.50	96.37(5)	96.18
$\gamma$	101.40(5)	102.4	98.07(5)	99.83
$\delta$	175.07(6)	173.39	175.30(5)	173.70

The calculated relative free energies of the *tb* and *hc* conformers is rather small, favoring the *tb* form over the *hc* one by only 0.96 kJ mol<sup>-1</sup>. This free energy difference provides an equilibrium constant at 298 K  $K = x_{hc}/x_{tb} = 0.68$  using  $\Delta G = -RT \ln K$ , which corresponds to a molar fraction of *hc* conformer  $x_{hc} = 0.40$  and thus a 2:3 (*hc:tb*) ratio of the two conformers in aqueous solution at 298 K. The interconversion between the *tb* and the *hc* conformers requires a change in the conformation of the six-membered chelate ring formed upon coordination of the trimethylenediamine moiety. The *tb* conformer is characterized by two identical CH<sub>2</sub>( $\alpha$ )–CH<sub>2</sub>( $\beta$ )–CH<sub>2</sub>( $\alpha$ )–N dihedral angles of  $-37.3^\circ$  due to the C<sub>2</sub> molecular symmetry, while in the *hc* form these dihedral angles amount to  $66.7^\circ$  and  $-86.8^\circ$ . The transition state responsible for the interconversion between the two forms is characterized by intermediate values of these angles ( $26.6^\circ$  and  $-78.79^\circ$ ) with one of the CH<sub>2</sub>( $\beta$ )–CH<sub>2</sub>( $\alpha$ ) units in a nearly eclipsed conformation (Figure S9, Supporting Information). According to our calculations the activation free energy for *tb*  $\rightleftharpoons$  *hc* interconversion is 13.5 kJ mol<sup>-1</sup>.

This energy barrier is very low, and significantly higher activation energies were estimated for the inversion of five-membered chelate rings in Ni<sup>2+</sup> complexes with ethylenediamine (20–29 kJ·mol<sup>-1</sup>)<sup>51</sup> and N,N,N',N'-tetramethylenediamine (32 kJ·mol<sup>-1</sup>).<sup>52</sup> Thus, the interconversion of the *tb* and *hc* conformers present in solution is expected to be fast in the NMR time scale, and consequently, NMR signals showing this interconversion (i.e., <sup>13</sup>C shifts of CH<sub>2</sub>( $\alpha$ ) and CH<sub>2</sub>( $\beta$ )) could not be resolved, even with a 600 MHz NMR instrument. As a consequence, the <sup>13</sup>C NMR shifts observed in D<sub>2</sub>O solutions

correspond to weighted averages of the chemical shifts of the *tb* and *hc* conformers.

The low energy barrier obtained from DFT calculations for the *tb*  $\rightarrow$  *hc* interconversion indicates that the dynamic process observed in the <sup>13</sup>C NMR spectra is related to a different exchange event. Most likely this is related to an intramolecular exchange process leading to a  $\Delta \rightleftharpoons \Lambda$  enantiomerization, which involves rotation of the acetate groups of the ligand that exchanges the in-plane and out-of-plane carboxylate units. This process might proceed intramolecularly following a concerted rotation of the four acetate groups of the ligand or it may be assisted by solvent exchange processes, as proposed for [Al(edta)]<sup>-</sup>.<sup>53</sup> DFT calculations were used to model the intramolecular  $\Delta \rightleftharpoons \Lambda$  interconversion process. The TS responsible for the interconversion between the  $\Delta$  and the  $\Lambda$  forms presents a trigonal prismatic coordination around the Ni<sup>II</sup> ion with a very long Ni–N distance of 2.71 Å (Figure S9 and Table S3, Supporting Information). The free energy of activation calculated for this process (79.4 kJ mol<sup>-1</sup>) is significantly higher than the one obtained from analysis of the <sup>13</sup>C NMR data (64.2 kJ mol<sup>-1</sup>), which suggests that the  $\Delta \rightleftharpoons \Lambda$  interconversion in [Ni(tmdta)]<sup>2-</sup> is assisted by the coordination of a water molecule, either with opening of a glycinate chelate ring or through a seven-coordinate intermediate.

The <sup>13</sup>C NMR chemical shifts of [Ni(tmdta)]<sup>2-</sup> are the result of both diamagnetic and paramagnetic contributions. The diamagnetic contribution in the case of paramagnetic lanthanide (Ln<sup>3+</sup>) complexes is often estimated from the chemical shifts observed for diamagnetic analogues such as La<sup>3+</sup> or Lu<sup>3+</sup> complexes.<sup>54</sup> The trivalent Ln<sup>3+</sup> ions represent a group of metal ions that are very similar in terms of their coordination chemistry, and therefore, this assumption is clearly justified. In the case of Ni<sup>2+</sup> complexes diamagnetic shifts could be estimated from the chemical shifts of the free ligand, but this would neglect the contribution to the diamagnetic shifts caused by conformational changes, inductive effects, and direct field effects related to complexation. Alternatively, the diamagnetic shifts could be estimated from the <sup>13</sup>C NMR shifts observed for [Zn(tmdta)]<sup>2-</sup>, assuming that the Ni<sup>2+</sup> and Zn<sup>2+</sup> complexes adopt similar structures. The X-ray structures published for different salts of the [Zn(tmdta)]<sup>2-</sup> complex indeed show that the Ni<sup>2+</sup> and Zn<sup>2+</sup> complexes of tmdta have very similar structures. The Zn<sup>2+</sup> complex was shown to adopt a *tb* conformation in the solid state.<sup>17</sup> Thus, we performed geometry optimizations of both the *tb* and *hc* conformers of [Zn(tmdta)]<sup>2-</sup> at the TPSSH/TZVP level and calculated the <sup>13</sup>C NMR shifts of each conformer using the GIAO method (Table 4). This method has been shown to provide theoretical

**Table 4. Experimental and Calculated <sup>13</sup>C NMR Shifts (ppm) and Hyperfine Coupling Constants (A<sub>iso</sub>, MHz) of [Ni(tmdta)]<sup>2-</sup>, and Calculated <sup>13</sup>C NMR Shifts of [Zn(tmdta)]<sup>2-</sup>**

	$\delta_{\text{Ni}}^{\text{exp}a}$	$\delta_{\text{Ni}}^{\text{calc}b}$	$\delta_{\text{Zn}}^{\text{calc}c}(\text{tb})$	$\delta_{\text{Zn}}^{\text{calc}c}(\text{hc})$	A <sub>iso</sub> ( <i>tb</i> )	A <sub>iso</sub> ( <i>hc</i> )
$\beta$ CH <sub>2</sub>	99.3	131.8	27.3	27.8	0.167	0.668
R COO <sup>-</sup>	21.7	40.1	180.0	180.1	-0.315	-0.756
G COO <sup>-</sup>	-91.5	-106.6	179.3	180.3	-1.010	-0.984
G CH <sub>2</sub> COO <sup>-</sup>	-436.4	-427.8	68.4	64.9	-1.732	-1.722
$\alpha$ CH <sub>2</sub>	-369.9	-393.0	55.7	63.2	-1.671	-1.434
R CH <sub>2</sub> COO <sup>-</sup>	-290.5	-254.8	58.7	64.7	-1.076	-1.145

<sup>a</sup>Experimental <sup>13</sup>C NMR shifts obtained at 293 K. <sup>b</sup>Calculated <sup>13</sup>C NMR shifts obtained with A<sub>iso</sub> values obtained for the *tb* and *hc* conformers, and diamagnetic shifts estimated for the Zn<sup>2+</sup> analogues. <sup>c</sup><sup>13</sup>C NMR shifts of [Zn(tmdta)]<sup>2-</sup> obtained with the GIAO method.

$^{13}\text{C}$  NMR shifts in good agreement with the experimental values for different  $\text{Zn}^{2+}$  complexes.<sup>55</sup> The  $^{13}\text{C}$  NMR spectrum of  $[\text{Zn}(\text{tmdta})]^{2-}$  has been reported previously but showed averaged signals for the methylene carbon of the exchanging in-plane and out-of-plane acetate groups (64.5 ppm) and a single averaged carboxylate resonance (181.3 ppm).<sup>56</sup> Our results (Table 4) show that the *tb* and *hc* forms present very similar chemical shifts, the larger chemical shift differences being predicted for the  $^{13}\text{C}$  NMR signals of the  $\alpha$   $\text{CH}_2$  and R  $\text{CH}_2\text{COO}^-$  nuclei (7.5 and 6.0 ppm, respectively).

In recent works it has been demonstrated that DFT calculations provide  $^1\text{H}$  and  $^{17}\text{O}$  hyperfine coupling constants of water molecules directly coordinated to  $\text{Mn}^{2+}$  and  $\text{Gd}^{3+}$  in very good agreement with the experimental data.<sup>57</sup> In the case of  $\text{Gd}^{3+}$  complexes calculation of  $^1\text{H}$   $A^{\text{iso}}$  values also allowed us to calculate contact shifts for the  $\text{Tb}^{3+}$  analogues.<sup>58</sup> Analogous calculations performed on the *tb* and *hc* conformers of  $[\text{Ni}(\text{tmdta})]^{2-}$  provided the  $A^{\text{iso}}$  values given in Table 4. The  $A^{\text{iso}}$  values obtained for the  $\beta$   $\text{CH}_2$  and R  $\text{COO}^-$  nuclei of the two conformers differ significantly, and therefore, the  $^{13}\text{C}$  NMR signals of these nuclei encode structural information that can be used to determine the relative populations of the conformers in solution. The calculated hyperfine coupling constants are all negative, except those corresponding to the  $\beta$   $\text{CH}_2$  nucleus, which are positive. The presence of alternate spin density (shift) signs along the pathway of the bonded atoms radiating out from the paramagnetic atom is a characteristic pattern that indicates that the contact shifts are dominated by spin polarization effects rather than spin delocalization.<sup>59</sup> Spin polarization is the result of an effective attraction of unpaired electrons to the nearby ones of the same spin. The  $\beta$  carbon of the propyl unit is three bonds away from the  $\text{Ni}^{2+}$  ion, while the remaining carbon nuclei of the ligand backbone are situated two bonds away from the paramagnetic center. Thus, the  $^{13}\text{C}$  NMR shifts of  $[\text{Ni}(\text{tmdta})]^{2-}$  appear to be dominated by spin-polarization effects. This is in line with the signs of the hyperfine coupling constants determined experimentally for  $\alpha$  and  $\beta$  carbon nuclei of simple amino acids in the presence of  $\text{Ni}^{2+}$ .<sup>60</sup>

The calculated  $A^{\text{iso}}$  values calculated for the *tb* and *hc* conformers of  $[\text{Ni}(\text{tmdta})]^{2-}$  were used to assess the relative abundance of these species in solution. For this purpose, we performed a least-squares fit that minimizes the difference between the experimental and calculated  $\delta_{i\text{Ni}}^{\text{exp}}$  values as given by the following expression

$$\delta_{i\text{Ni}} = F[x_{tb}A_{i,tb}^{\text{iso}} + (1 - x_{tb})A_{i,hc}^{\text{iso}}] + x_{tb}\delta_{i\text{Zn},tb}^{\text{calcd}} + x_{tb}\delta_{i\text{Zn},hc}^{\text{calcd}} \quad (4)$$

where the fitting parameters are the molar fraction of *tb* isomer,  $x_{tb}$ , and the proportionality constant  $F$  (eq 3). In this equation  $A_{i,tb}^{\text{iso}}$  represents the calculated hyperfine coupling constant of a nucleus  $i$  of the *tb* conformer (in MHz), and  $\delta_{i\text{Zn},tb}^{\text{calcd}}$  is the chemical shift of nucleus  $i$  obtained for the *tb* isomer of  $[\text{Zn}(\text{tmdta})]^{2-}$  with GIAO calculations. The best fit of the data provided the calculated shifts reported in Table 4, with  $x_{tb} = 0.60 \pm 0.14$  and  $F = 286.0 \pm 10.0$ . The agreement between the experimental and calculated  $^{13}\text{C}$  NMR shifts is quite good, with an agreement factor  $AF_i = 0.090$ .<sup>61</sup> Furthermore, the value of  $F$  obtained from the fit is in excellent agreement with the theoretical value obtained with eq 3 at 293 K (285.9). In addition, the molar fraction of *tb* conformer is in good agreement with the IR and Raman studies described below. Therefore, we conclude that (i) our DFT calculations provide

accurate  $^{13}\text{C}$  hyperfine coupling constants, (ii) the paramagnetic shifts of  $[\text{Ni}(\text{tmdta})]^{2-}$  are largely dominated by the contact contribution, and (iii) our combined NMR and DFT approach allows for an accurate determination of the relative populations of *tb* and *hc* conformers in aqueous solution.

**Vibrational Spectroscopy.** IR spectra of a 0.6 M aqueous solution of  $\text{Li}_2[\text{Ni}(\text{tmdta})]$  **1a** could be obtained in the range 1000–1250  $\text{cm}^{-1}$  (Figure 5). The spectrum is compared with

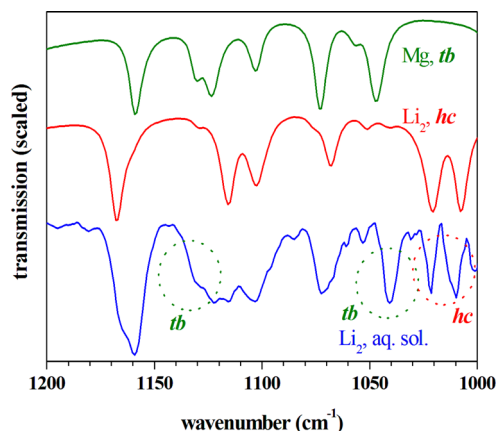


**Figure 5.** IR spectra obtained from solid samples of the  $\text{Li}^+$  and  $\text{Mg}^{2+}$  salts of  $[\text{Ni}(\text{tmdta})]^{2-}$ , and IR spectrum obtained for the  $\text{Li}^+$  salt in aqueous solution (0.6 M). Circles highlight regions of the IR spectrum in solution that point to the presence of both the *tb* and the *hc* conformers.

those recorded in the solid state for the  $\text{Li}_2[\text{Ni}(\text{tmdta})]$  and  $\text{Mg}[\text{Ni}(\text{tmdta})]$  salts, which provide *hc* and *tb* conformations, respectively (see above). The spectrum of the  $\text{Li}^+$  salt presents two features at 1008 and 1020  $\text{cm}^{-1}$ , assigned to rocking vibrations of the methylene groups,  $\rho(\text{CH}_2)$ . The spectrum of the  $\text{Mg}^{2+}$  salt, which adopts a *tb* conformation, shows the band due to the  $\rho(\text{CH}_2)$  vibration at 1046  $\text{cm}^{-1}$ , quite well separated from those observed for the  $\text{Li}^+$  salt. Thus, these bands can provide information on the relative populations of the *tb* and *hc* conformers present in solution. The IR spectrum obtained for the  $\text{Li}^+$  salt in aqueous solution shows bands at 1010, 1021, and 1041  $\text{cm}^{-1}$  that clearly identify the presence of both conformers in solution with significant populations.

The geometries of the *tb* and *hc* conformers of  $[\text{Ni}(\text{tmdta})]^{2-}$  optimized at the TPSSH/TZVP level were used to calculate the corresponding vibrational wavenumbers within the harmonic approach. Calculated spectra are compared with the spectrum recorded in aqueous solution in Figure 6, while the positions of the calculated bands are compared to the experimental data of the  $\text{Li}^+$  and  $\text{Mg}^{2+}$  salts in Table 5. Our calculations provide unscaled vibrational frequencies in excellent agreement with those observed in the solid state. A comparison of the calculated spectra with the experimental spectrum obtained in solution clearly confirms that the two conformers have sizable populations in water.

In order to obtain quantitative information on the relative abundance of the *tb* and *hc* forms in aqueous solution, we performed simulations of the experimental solution spectrum using linear combinations of the spectra calculated for the two conformers. A similar approach has been shown to allow determining accurately the *tb*/*hc* ratio using DFT-calculated Raman spectra.<sup>15</sup> The experimental spectrum recorded in

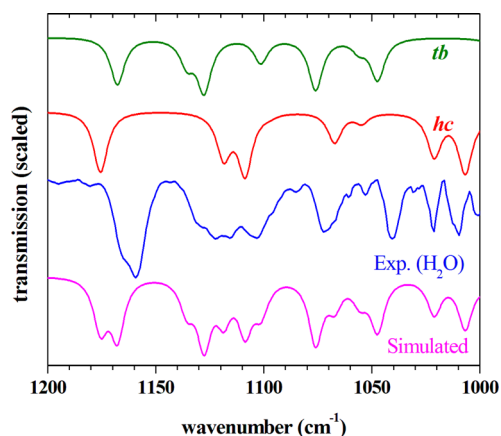


**Figure 6.** IR spectra of the *tb* and *hc* conformers of  $[\text{Ni}(\text{tmdta})]^{2-}$  obtained with theoretical TPSSh/TZVP calculations, experimental IR spectrum obtained for the  $\text{Li}^+$  salt in aqueous solution (0.6 M), and simulated solution spectrum obtained with the theoretical spectra of the *tb* and *hc* conformers assuming a 2:3 *hc:tb* ratio.

**Table 5. Experimental and Calculated (TPSSh/TZVP) IR Bands ( $\text{cm}^{-1}$ ) of  $[\text{Ni}(\text{tmdta})]^{2-}$**

conformer	exp.	calcd	intensity <sup>a</sup>	assignment
<i>hc</i>	1008	1007	41.0	$\rho(\text{CH}_2)$
	1020	1021	29.9	$\rho(\text{CH}_2)$
	1068	1067	21.6	$\nu(\text{C}-\text{C})$
	1103	1109	43.0	$\nu(\text{N}-\text{CH}_2\text{CH}_2)$
	1116	1119	31.0	$\nu(\text{N}-\text{CH}_2\text{CH}_2)$
	1168	1176	43.1	$\nu(\text{N}-\text{CH}_2\text{COO}^-)$
<i>tb</i>	1046	1047	29.3	$\rho(\text{CH}_2)$
	1072	1076	36.7	$\nu(\text{C}-\text{C})$
	1102	1101	17.5	$\nu(\text{N}-\text{CH}_2\text{COO}^-)$
	1124	1128	37.0	$\nu(\text{N}-\text{CH}_2\text{CH}_2)$
	1130	1136	17.3	$\nu(\text{N}-\text{CH}_2\text{CH}_2)$
	1159	1168	33.5	$\nu(\text{N}-\text{CH}_2\text{COO}^-)$

<sup>a</sup>Calculated IR intensity ( $\text{km mol}^{-1}$ ).

aqueous solution could be accurately simulated using a *hc:tb* ratio of 2:3 (Figure 6). The bands observed at 1010 and 1021  $\text{cm}^{-1}$  in the solution spectrum arise from rocking vibrations of the methylene groups [ $\rho(\text{CH}_2)$ ] of the *hc* conformer, while the band at 1041  $\text{cm}^{-1}$  is associated with the same vibrational mode of the *tb* form. The spectral region 1060–1200  $\text{cm}^{-1}$  presents mixtures of  $\nu(\text{C}-\text{C})$  and  $\nu(\text{N}-\text{C})$  stretching modes of the two conformers.

The Raman spectrum of the  $\text{Li}^+$  salt of  $[\text{Ni}(\text{tmdta})]^{2-}$  was obtained in aqueous solution in the region 300–600  $\text{cm}^{-1}$ . As noticed before, the Fe–O and Fe–N stretching modes and skeletal vibrations of the coordination polyhedron are observed in this region.<sup>62</sup> The spectrum recorded in solution (Figure 7) is dominated by two bands at 438 and 510  $\text{cm}^{-1}$  and presents bands of lower intensity at 468, 403, and 360  $\text{cm}^{-1}$ . A comparison of the calculated Raman spectra with the spectrum measured in aqueous solution shows that the main features of the latter are likely to have significant contributions of the two conformers. The theoretical spectrum simulated from the calculated Raman spectra and intensities using a *hc:tb* ratio of 2:3 present excellent agreement with the experimental spectrum, which confirms the predictions made on the basis of the IR spectra. Calculated Raman peaks and intensities for the two isomers and their assignments are compiled in Table 6.

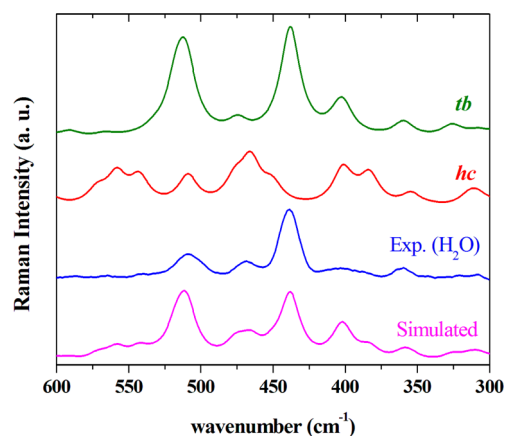


**Figure 7.** Raman spectra of the *tb* and *hc* conformers of  $[\text{Ni}(\text{tmdta})]^{2-}$  obtained with theoretical TPSSh/TZVP calculations, experimental Raman spectrum obtained for the  $\text{Li}^+$  salt in aqueous solution (0.6 M), and simulated solution spectrum obtained with the theoretical spectra of the *tb* and *hc* conformers assuming a 2:3 *hc:tb* ratio.

**Table 6. Calculated (TPSSh/TZVP) Raman Bands ( $\text{cm}^{-1}$ ) and Intensities of  $[\text{Ni}(\text{tmdta})]^{2-}$**

conformer	no.	calcd	intensity <sup>a</sup>	assignment	
<i>hc</i>	32	572	3.5	$\pi(\text{C}=\text{O}) + \rho(\text{CH}_2)$	
	31	558	7.0	$\pi(\text{C}=\text{O}) + \rho(\text{CH}_2)$	
	30	543	6.3	$\pi(\text{C}=\text{O}) + \rho(\text{CH}_2)$	
	29	509	6.9	$\nu(\text{Ni}-\text{N}) + \rho(\text{CH}_2)$	
	28	476	5.2	Gly $\rho(\text{CH}_2)$	
	27	465	9.9	Gly $\rho(\text{CH}_2)$	
	26	451	4.4	Gly + ring $\rho(\text{CH}_2)$	
	25	402	8.2	Gly $\rho(\text{CH}_2)$	
	24	394	0.7	Gly + ring $\rho(\text{CH}_2)$	
	23	383	6.9	Gly $\rho(\text{CH}_2)$ + ring bend	
	22	354	2.8	$\nu(\text{Ni}-\text{O})$ + ring bend	
	20	314	2.2	Gly $\rho(\text{CH}_2)$ + ring $\rho(\text{CH}_2)$	
	19	308	2.3	Gly $\rho(\text{CH}_2)$	
	<i>tb</i>	33	591	1.4	$\pi(\text{C}=\text{O}) + \rho(\text{CH}_2)$
		32	566	0.8	$\pi(\text{C}=\text{O}) + \rho(\text{CH}_2)$
		31	532	0.9	$\pi(\text{C}=\text{O}) + \rho(\text{CH}_2)$
		30	517	11.1	$\nu(\text{Ni}-\text{N}) + \rho(\text{CH}_2)$
		39	510	11.9	$\nu(\text{Ni}-\text{N})$
		28	510	3.8	$\nu(\text{Ni}-\text{N}) + \rho(\text{CH}_2)$
27		475	3.0	$\nu(\text{Ni}-\text{N}) + \rho(\text{CH}_2)$	
26		438	25.3	ring twist	
25		405	2.8	Gly $\rho(\text{CH}_2)$	
24		401	5.6	Gly $\rho(\text{CH}_2)$	
23	360	3.3	ring deformation		
21	326	2.3	$\nu(\text{Ni}-\text{O})$ + ring bend		
19	308	1.2	$\nu(\text{Ni}-\text{O})$ + ring bend		

<sup>a</sup>Calculated Raman intensity ( $\text{\AA}^4/\text{amu}$ ).

Analysis of the calculated Raman spectra shows that this region has a contribution of a large number of vibrational modes, including out of plane deformations of the carboxylate groups [ $\pi(\text{C}=\text{O})$ ], rocking vibrations of the methylene groups [ $\rho(\text{CH}_2)$ ], sometimes coupled to  $\nu(\text{Ni}-\text{N})$  stretching vibrations, and deformations of the six-membered chelate ring formed upon coordination of the propylenediamine unit.

**Electronic Spectra of  $[\text{Ni}(\text{tmdta})]^{2-}$  Salts in the Solid State and in Aqueous Solution.** As shown in Figure 8 (for band positions see Table 7), the solid state spectra of both *hc*

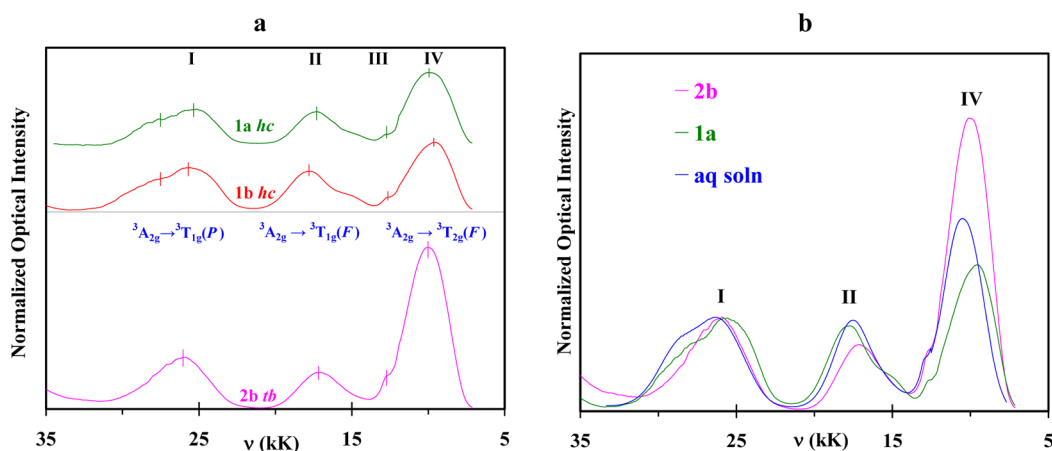


**Figure 8.** (a) Comparison of the solid state reflection spectra recorded for **1a**, **1b**, and **2b**. (b) Aqueous solution spectrum of  $[\text{Ni}(\text{tmdta})]^{2-}$  as compared with the solid state spectra of **1a** and **2b**. To enable comparison of relative intensities, spectra were normalized to have all the same intensities at band.

**Table 7. Data Describing Band Positions and Intensities in Solid State and Solution UV/Vis/NIR Spectra of 1a, 1b, and 2b and the Spectrum of  $[\text{Ni}(\text{tmdta})]^{2-}$  in Aqueous solution**

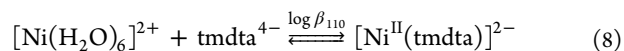
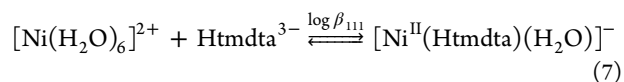
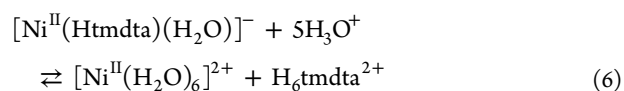
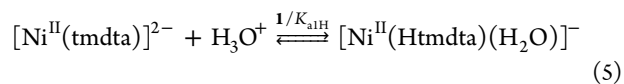
transition ( $O_h$ )	$\nu$ in $\text{kK} = \text{cm}^{-1} \times 10^{-3}$ (nm) $\{\epsilon$ ( $\text{M}^{-1} \text{cm}^{-1}$ ) $\}$			
	<b>1a</b>	<b>1b</b>	<b>2b</b>	aq soln
band I ( ${}^3\text{A}_{2g} \rightarrow {}^3\text{T}_{1g}(\text{P})$ )	27.51 (364) sh	27.51 (364) sh		27.86 (359) sh {7.37}
	25.35 (394)	25.70 (389)	26.04 (389)	26.32 (380) {8.53}
band II ${}^3\text{A}_{2g} \rightarrow {}^3\text{T}_{1g}(\text{F})$	17.30 (578)	17.80 (562)	17.18 (582)	17.54 (570) {8.28}
band III ${}^3\text{A}_{2g} \rightarrow {}^1\text{E}_{1g}(\text{D})$	12.72 (786)	12.64 (791)	12.73 (786)	12.67 (789) {5.23}
band IV ( ${}^3\text{A}_{2g} \rightarrow {}^3\text{T}_{2g}(\text{F})$ )	9.95 (1005)	9.64 (1037)	10.02 (999)	10.54 (949) {17.52}

salts **1a** and **1b** differ considerably from that of *tb* salt **2b**. While the relative intensities of the transitions at higher energies (I  ${}^3\text{A}_{2g} \rightarrow {}^3\text{T}_{1g}(\text{P})$ , II  ${}^3\text{A}_{2g} \rightarrow {}^3\text{T}_{1g}(\text{F})$ ) are roughly the same for the *tb* and *hc* isomers, the large intensity difference of band IV ( ${}^3\text{A}_{2g} \rightarrow {}^3\text{T}_{2g}(\text{F})$  transition) for *hc* and *tb* isomers (*hc* intensity is only one-half the *tb* one at position of this band) is unexpected and there is no example in the current literature for any similar observation. We assume that lowering in the symmetry described in the solid structures of **1a** and **1b** (described in the structure section above) is responsible for the low intensity of the 10 Dq band in the *hc* spectra.

Interesting is the comparison shown in Figure 8b where the solid state spectra of **1a** and **2b** are compared with the unique solution spectrum of  $[\text{Ni}(\text{tmdta})]^{2-}$  (the solution spectrum is not dependent upon whether *tb* or *hc* is dissolved). As observed before, the intensity of the 10 Dq band in the case of the solution spectrum is reflecting the presence of a *tb*/*hc* equilibrium mixture in aqueous solutions.

**Estimation of Complex Stability Constant  $\log \beta_{110}$  and  $\text{p}K_{\text{a1H}}$  for  $\text{Ni}^{\text{II}}\text{-tmdta}$ .** In previous works we have shown that pH-dependent spectrophotometric titration experiments can be applied to estimate various types of equilibrium constants<sup>47,63</sup> with the aid of the SPECFIT software developed by Zuberbühler et al.<sup>64</sup> Titration of water-soluble metal chelate complexes with acid accompanied by pH lowering delivers usually equilibrium constants for complex formation and stepwise protonation constants of appropriate complexes. The conditional equilibrium expressions for the relevant processes valid for  $\text{Ni}^{\text{II}}\text{-tmdta}$  are given in eqs 5 and 6, while the mass balance equations required for quantitative analysis are formulated in eqs 7 and 8. The spectrum of the neutral solution containing  $[\text{Ni}^{\text{II}}(\text{tmdta})]^{2-}$  is gradually changed upon

addition of  $\text{HClO}_{4\text{conc}}$  in small aliquots as shown in Figure 9a. A fit to the spectra shown in Figure 9a applying SPECFIT and a three-component model (species  $[\text{Ni}^{\text{II}}(\text{tmdta})]^{2-}$ ,  $[\text{Ni}^{\text{II}}(\text{Htmdta})(\text{H}_2\text{O})]^-$ , and  $[\text{Ni}^{\text{II}}(\text{H}_2\text{O})_6]^{2+}$ ) delivers the results shown in Figure 9b and 9c and Table 8. The data reported in Table 8 reveals a good agreement between our constants and those given in the literature, in particular considering that the literature values were determined at an ionic strength  $I = 0.1 \text{ M}$  ( $\text{K}^+$  containing supporting electrolyte,  $25^\circ\text{C}$ ) while our data were measured at an ionic strength of  $I = 1.0 \text{ M}$   $\text{NaClO}_4$ ,  $25^\circ\text{C}$ .



Our  $\text{p}K_{\text{a1H}}$  for the protonation of  $[\text{Ni}^{\text{II}}(\text{tmdta})]^{2-}$  (reverse process of reaction 5) is considerably lower than the one originally estimated by Anderegg.<sup>65</sup> In the latter work, equilibrium data were measured by pH potentiometry at  $20^\circ\text{C}$ ,  $I = 0.1 \text{ M}$  ( $\text{KNO}_3$ ). The authors state that the  $\text{p}K_{\text{a1H}}$  value they evaluated can contain large errors. The  $\text{p}K_{\text{a1H}} = 2.69$  that we evaluated for  $\text{Ni}^{\text{II}}\text{-tmdta}$  is in very good agreement with one given by Higginson<sup>66</sup> ( $\text{p}K_{\text{a1H}} = 2.63$ ), who used spectrophotometric titrations for his measurements and solution conditions

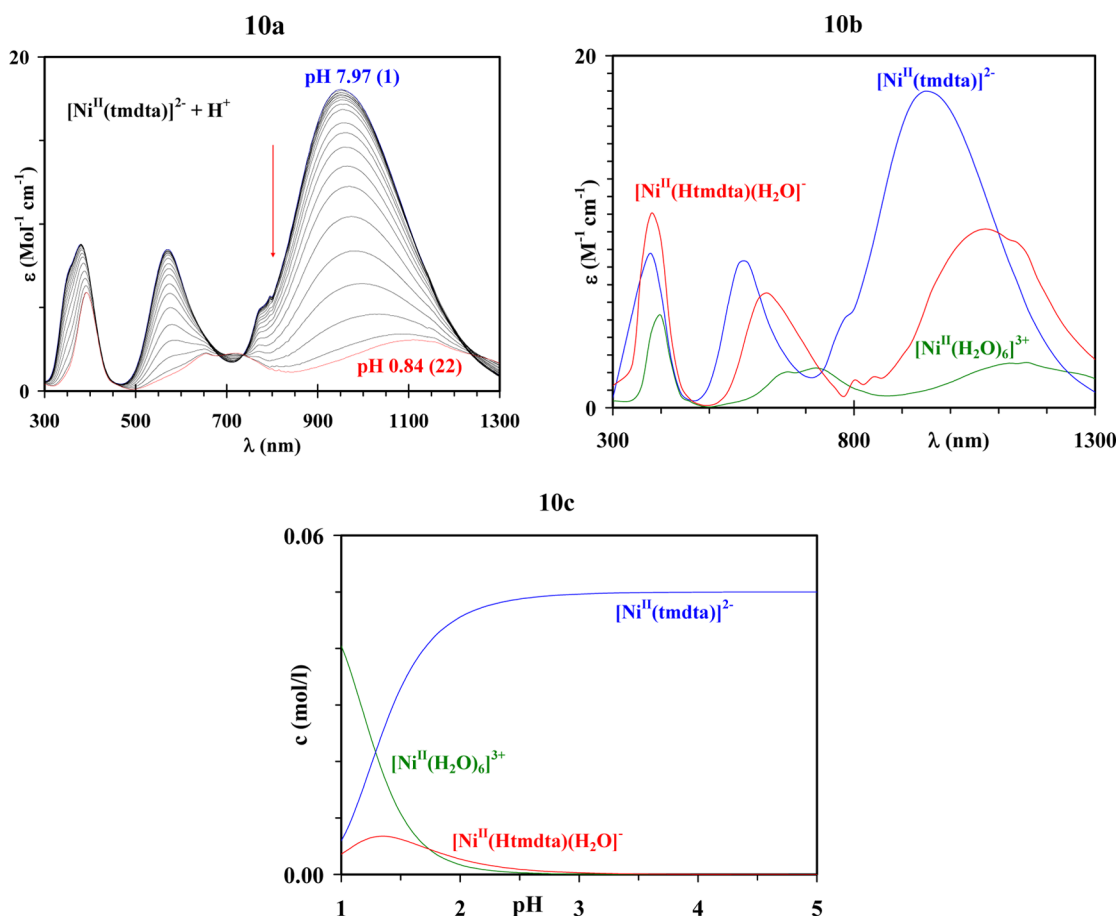


**Figure 9.** (a) Spectral changes of 0.05 M  $[\text{Ni}^{\text{II}}(\text{tmdta})]^{2-}$  ( $I = 1.0$  M  $\text{NaClO}_4$ , 25 °C, metal-to-ligand ratio 1:1) upon addition of small amounts of  $\text{HClO}_{4\text{conc}}$ . (b) Limiting spectra for  $[\text{Ni}^{\text{II}}(\text{tmdta})]^{2-}$ ,  $[\text{Ni}^{\text{II}}(\text{Htmdta})(\text{H}_2\text{O})]^-$ , and  $[\text{Ni}(\text{H}_2\text{O})_6]^{2+}$  obtained upon evaluation of the equilibrium constants given in Table 8 with SPECFIT. (c) pH-dependent distribution of  $[\text{Ni}^{\text{II}}(\text{tmdta})]^{2-}$ ,  $[\text{Ni}^{\text{II}}(\text{Htmdta})(\text{H}_2\text{O})]^-$ , and  $[\text{Ni}(\text{H}_2\text{O})_6]^{2+}$  in the range  $1 < \text{pH} < 5$ .

**Table 8. Comparison of Equilibrium for Complex Formation and Protonation for  $\text{Ni}^{\text{II}}\text{-tmdta}$  and  $\text{Ni}^{\text{II}}\text{-edta}$  ( $I = 1.0$  M  $\text{NaClO}_4$ , 25 °C)<sup>a</sup>**

equilibrium constant	$\text{Ni}^{\text{II}}\text{-tmdta}$	$\text{Ni}^{\text{II}}\text{-edta}$
$\log \beta_{110}$	$18.64 \pm 0.01$ (18.21)	$18.28 \pm 0.02$ ( $18.4 \pm 0.1$ )
$\log \beta_{111}$	$19.42 \pm 0.02$	$20.97 \pm 0.02$
$\text{p}K_{\text{a1H}}$	0.78 (~2.2)	2.69 ( $3.0 \pm 0.1$ )

<sup>a</sup>The ligand  $\text{p}K_{\text{a}}$  data used during SPECFIT application are collected in Table S4, Supporting Information. Values in parentheses are those given in ref.<sup>67</sup> for 25 °C,  $I = 0.1$  M.

identical with ours ( $I = 1.0$  M  $\text{NaClO}_4$ , 25 °C). This shows that our approach is suitable to gain reliable data. A surprising feature of these equilibrium constants that needs explanation is the gap between  $\text{p}K_{\text{a1H}} = 0.78$  for  $\text{Ni}^{\text{II}}\text{-tmdta}$  compared to  $\text{p}K_{\text{a1H}} = 2.69$  for  $\text{Ni}^{\text{II}}\text{-edta}$ . We have shown in previous work<sup>3</sup> that both  $\text{Ni}^{\text{II}}\text{-edta}$  and  $\text{Ni}^{\text{II}}\text{-tmdta}$  contain small amounts of a water-coordinated complex species. As shown before,<sup>56</sup> any edta complex with CN 6 and a fully coordinated ligand contains a certain equilibrium amount of CN 7 species with a coordinated water. For the current case, i.e., protonation of  $[\text{Ni}^{\text{II}}(\text{edta})]^{2-}$ , the active species accepting the proton could be seven-coordinate  $[\text{Ni}^{\text{II}}(\text{edta})(\text{H}_2\text{O})]^{2-}$ . The amount of seven-coordinate fraction in the case of  $\text{Ni}^{\text{II}}\text{-tmdta}$  should be considerably smaller than with  $\text{Ni}^{\text{II}}\text{-edta}$ , because of stereochemical reasons.<sup>3,56</sup> This difference is likely responsible for the

different  $\text{p}K_{\text{a1H}}$  values (almost two log units) observed for  $\text{Ni}^{\text{II}}\text{-tmdta}$  and  $\text{Ni}^{\text{II}}\text{-edta}$ .

## CONCLUSIONS

Our study shows in a clear-cut way an adequate strategy to quantify a  $tb \rightleftharpoons hc$  equilibrium between labile  $\text{Ni}^{\text{II}}$  complex species in solution. Experimental structures obtained with X-ray diffraction measurements and DFT-optimized geometries provided limiting structures that served as basis to establish the equilibrium ratio of 40%  $hc$  and 60%  $tb$ . The latter was estimated by systematic comparisons of experimental IR and Raman spectra with those computed with DFT calculations. Our NMR spectral results are of special interest because it was established for the very first time in a edta-type complex that the  $\lambda \rightleftharpoons \delta$  glycinate chelate ring interconversions take place with a velocity that is 2 orders of magnitude slower than the analogous process in the central diamine T ring. Furthermore, we developed an approach to determine the solution structure of  $\text{Ni}^{2+}$  complexes by analyzing the experimental <sup>13</sup>C NMR shifts with the aid of DFT calculations. Our results show that the paramagnetic shifts induced by  $\text{Ni}^{2+}$  are dominated by the contact contribution, which can be obtained in a straightforward way by computing isotropic hyperfine coupling constants with the aid of DFT calculations. The contact shifts calculated for the  $tb$  and  $hc$  isomers are significantly different and therefore can be used to gain information on the populations of these

conformers in solution. Analysis of the contact shifts confirms the 40% *hc* and 60% *tb* population obtained from analysis of the IR and Raman spectra.

Recording of solid state and solution spectra of *hc* and *tb* complexes reveals that the *tb* form shows a much greater intensity of the 10 Dq band ( ${}^3A_{2g} \rightarrow {}^3T_{2g}(F)$  transition) than the *hc*, while the common solution spectrum reflects again the presence of a  $tb \rightleftharpoons hc$  equilibrium in solution. Equilibrium measurements clarify that  $[Ni(tmdta)]^{2-}$  has about the same complex stability compared to  $Ni(edta)]^{2-}$ , but the former shows a much greater resistance against protonation as compared to the latter.

We believe that the methodology reported in this work represents a valuable tool to establish the solution structures of  $Ni^{2+}$  as well as other transition metal complexes with polyaminocarboxylate ligands, an issue of crucial importance for a better understanding of the reactivity of this important class of compounds. Furthermore, we have shown that the NMR spectra of  $Ni^{2+}$  complexes are dominated by contact shifts that can be accurately predicted with DFT calculations. Extension of the methods reported here to other complexes will allow a more robust characterization of an innovative class of  $Ni^{2+}$ -based paramagnetic probes for magnetic resonance imaging that take advantage of the chemical exchange saturation transfer effect (ParaCEST).<sup>68</sup>

## ■ ASSOCIATED CONTENT

### ■ Supporting Information

Crystal data and structure refinement details, additional structural details, comparison of experimental and DFT structures, Dunitz plot for the *tb* structures, temperature dependence of the  ${}^{13}C$  NMR chemical shifts, views of the DFT-optimized structures of energy minima and transition states, optimized Cartesian coordinates of energy minima and transition states obtained with DFT computations and X-ray crystallographic data in CIF format. This material is available free of charge via the Internet at <http://pubs.acs.org>.

## ■ AUTHOR INFORMATION

### Corresponding Authors

\*E-mail: Roland.Meier@fau.de.

\*E-mail: carlos.platas.iglesias@udc.es.

### Notes

The authors declare no competing financial interest.

## ■ ACKNOWLEDGMENTS

C.P.-I. is indebted to Centro de Supercomputación de Galicia (CESGA) for providing the computer facilities. R.M. is grateful to the Alexander-von-Humboldt foundation and Dr. Steffen Mehlich who supported this study in its initial phase. Drs. Alexander Czaja and Jens Schönewerk recorded the solid state UV/vis/NIR spectra shown in here. Stefanie Worsch undertook most of the spectrophotometric work. Prof. C. J. Zhong (SUNY at Binghamton) and BayFor (Munich) enabled a stay of R.M. in the United States.

## ■ REFERENCES

(1) (a) Knepper, T. P. *Trends Anal. Chem.* **2003**, *10*, 708–724. (b) Suarez, L.; Garcia, R.; Riera, F. A.; Diez, M. A. *Talanta* **2013**, *115*, 652–656. (c) Kolodynska, D.; Hubicka, H.; Hubicki, Z. *Desalination* **2008**, *227*, 150–156. (d) Nowack, B.; VanBriese, J. M. In *Biogeochemistry of Chelating Agents*; ACS Symposium Series; American Chemical Society: Washington, DC, 2005.

(2) (a) Andersen, O. *Chem. Rev.* **1999**, *99*, 2683–2710. (b) Nlanusa, M.; Varnai, V. M.; Piasek, M.; Kostial, K. *Curr. Med. Chem.* **2005**, *12*, 2771–2794.

(3) Maigut, J.; Meier, R.; Zahl, A.; va Eldik, R. *J. Am. Chem. Soc.* **2008**, *130*, 14556–14569.

(4) Aime, S.; Botta, M.; Ermondi, G. *Inorg. Chem.* **1992**, *31*, 4291–4299.

(5) Desreux, J. F. *Inorg. Chem.* **1980**, *19*, 1319–1324.

(6) Aime, S.; Barge, A.; Botta, M.; De Sousa, A. S.; Parker, D. *Angew. Chem., Int. Ed.* **1998**, *37*, 2673–2675.

(7) Zhang, T.; Zhu, X.; Prabhakar, R. *Organometallics* **2014**, *33*, 1925–1935.

(8) Liang, X.; Weishaupl, M.; Parkinson, J. A.; Parsons, S.; McGregor, P. A.; Sadler, P. J. *Chem.—Eur. J.* **2003**, *9*, 4709–4717.

(9) Nagao, R.; Marumo, F.; Saito, Y. *Acta Crystallogr.* **1972**, *B28*, 1852–1856.

(10) Sun, D.-W.; Zhang, Q.; Zhai, H.-J. *Acta Crystallogr.* **2006**, *E62*, m2770–m2772.

(11) Herak, R.; Srdanov, G.; Djuran, M. I.; Radanovic, D. J.; Bruvo, M. *Inorg. Chim. Acta* **1984**, *83*, 55–64.

(12) Okamoto, K.; Kanamori, K.; Hidaka, J. *Acta Crystallogr.* **1990**, *C46*, 11640–1642.

(13) Robles, J. C.; Matsuzaka, Y.; Inomata, S.; Shimoi, M.; Mori, W.; Ogino, H. *Inorg. Chem.* **1993**, *32*, 13–17.

(14) Wang, J.; Gao, G. R.; Zhang, Z. H.; Zhang, X. D.; Liu, X. Z.; Kong, Y. M.; Li, Y. *Russ. J. Coord. Chem.* **2007**, *33*, 258–264.

(15) Meier, R.; Maigut, J.; Kallies, B.; Lehnert, N.; Paulat, F.; Heinemann, F. W.; Zahn, G.; Feth, M. P.; Krautscheid, H.; van Eldik, R. *Chem. Commun.* **2007**, 3960–3962.

(16) Radanovic, D. D.; Rychlewska, U.; Djuran, M. I.; Draskovic, N. S.; Vasojevic, M. M.; Hodid, I. M.; Radanovic, D. J. *Polyhedron* **2003**, *22*, 2745–2753.

(17) Rychlewska, U.; Guresic, D. M.; Warzajtis, B.; Radanovic, D. D.; Djuran, M. I. *Polyhedron* **2005**, *24*, 2009–2016.

(18) Radanovic, D. D.; Rychlewska, U.; Djuran, M. I.; Warzajtis, B.; Draskovic, N. S.; Guresic, D. M. *Polyhedron* **2004**, *23*, 2183–2192.

(19) Radanovic, D. J.; Ama, T.; Kawaguchi, H.; Draskovic, N. S.; Ristanovic, D. M.; Janicijevic, S. *Bull. Chem. Soc. Jpn.* **2001**, *74*, 701–706.

(20) Rychlewska, U.; Radanovic, D. D.; Jevtovic, V. S.; Radanovic, D. J. *Polyhedron* **2000**, *19*, 1–5.

(21) Hernandez-Padilla, M.; China, E.; Dominguez, S.; Mederos, A.; Munoz, M. C.; Lloret, F. *Polyhedron* **2000**, *19*, 1175–1179.

(22) Rychlewska, U.; Warzajtis, B.; Cvetic, D.; Radanovic, D. D.; Guresic, D. M.; Djuran, M. I. *Polyhedron* **2007**, *26*, 1717–1724.

(23) Wang, J.; Hu, P.; Liu, B.; Xu, R.; Wang, X.; Wang, D.; Zhang, X. D. *J. Struct. Chem.* **2011**, *52*, 568–574.

(24) Wang, J.; Hu, P.; Liu, B.; Chen, X.; Zhang, L. Q.; Han, G. X.; Xu, R.; Zhang, X. D. *Russ. J. Inorg. Chem.* **2010**, *55*, 1567–1573.

(25) Wang, J.; Hu, P.; Han, G.; Zhang, L.; Li, D.; Xu, R.; Chen, X.; Zang, X. D. *Zh. Strukt. Khim.* **2011**, *52*, 592.

(26) Liu, B.; Hu, P.; Wang, J.; Xu, R.; Zhang, L. Q.; Gao, J.; Wang, Y. F.; Zhang, X. D. *Koord. Khim.* **2009**, *35*, 768.

(27) Yamamoto, T.; Mikata, K.; Miyoshi, K.; Yoneda, H. *Inorg. Chim. Acta* **1988**, *150*, 237–244.

(28) Rychlewska, U.; Warzajtis, B.; Djuran, M. I.; Radanovic, D. D.; Dimitrijevic, M. D.; Rajkovic, S. *Acta Crystallogr.* **2008**, *C64*, m217–m220.

(29) Weyh, J. A.; Hamm, R. E. *Inorg. Chem.* **1968**, *7*, 2431–2435.

(30) *SHELXTL-NT*, Version 5.10, Bruker Analytical X-ray Systems, 1999.

(31) Frisch, M. J.; Trucks, G. W.; Schlegel, H. B.; Scuseria, G. E.; Robb, M. A.; Cheeseman, J. R.; Scalmani, G.; Barone, V.; Mennucci, B.; Petersson, G. A.; Nakatsuji, H.; Caricato, M.; Li, X.; Hratchian, H. P.; Izmaylov, A. F.; Bloino, J.; Zheng, G.; Sonnenberg, J. L.; Hada, M.; Ehara, M.; Toyota, K.; Fukuda, R.; Hasegawa, J.; Ishida, M.; Nakajima, T.; Honda, Y.; Kitao, O.; Nakai, H.; Vreven, T.; Montgomery, Jr., J. A.; Peralta, J. E.; Ogliaro, F.; Bearpark, M.; Heyd, J. J.; Brothers, E.; Kudin, K. N.; Staroverov, V. N.; Kobayashi, R.; Normand, J.; Raghavachari, K.

Rendell, A.; Burant, J. C.; Iyengar, S. S.; Tomasi, J.; Cossi, M.; Rega, N.; Millam, N. J.; Klene, M.; Knox, J. E.; Cross, J. B.; Bakken, V.; Adamo, C.; Jaramillo, J.; Gomperts, R.; Stratmann, R. E.; Yazyev, O.; Austin, A. J.; Cammi, R.; Pomelli, C.; Ochterski, J. W.; Martin, R. L.; Morokuma, K.; Zakrzewski, V. G.; Voth, G. A.; Salvador, P.; Dannenberg, J. J.; Dapprich, S.; Daniels, A. D.; Farkas, Ö.; Foresman, J. B.; Ortiz, J. V.; Cioslowski, J.; Fox, D. J. *Gaussian 09*, Revision A.01; Gaussian, Inc.: Wallingford, CT, 2009.

(32) Tao, J. M.; Perdew, J. P.; Staroverov, V. N.; Scuseria, G. E. *Phys. Rev. Lett.* **2003**, *91*, 146401.

(33) Schaefer, A.; Huber, C.; Ahlrichs, R. *J. Chem. Phys.* **1994**, *100*, 5829–5835.

(34) Stanton, J. F.; Gauss, J. *Adv. Chem. Phys.* **2003**, *125*, 101–146.

(35) Montoya, A.; Truong, T. N.; Sarofim, A. F. *J. Phys. Chem. A* **2000**, *124*, 6108–6110.

(36) (a) Peng, C.; Ayala, P. Y.; Schlegel, H. B.; Frisch, M. J. *J. Comput. Chem.* **1996**, *17*, 49–56. (b) Peng, C.; Schlegel, H. B. *Isr. J. Chem.* **1994**, *33*, 449–454.

(37) Orio, M.; Pantazis, D. A.; Neese, F. *Photosynth. Res.* **2009**, *102*, 443–453.

(38) Rega, N.; Cossi, M.; Barone, V. *J. Chem. Phys.* **1996**, *105*, 11060–11067.

(39) Neese, F. *Coord. Chem. Rev.* **2009**, *253*, 526–563.

(40) Bertini, I.; Luchinat, C. *Coord. Chem. Rev.* **1996**, *150*, 29–75.

(41) Ditchfield, R. *Mol. Phys.* **1974**, *27*, 789–807.

(42) Dennington, R.; Keith, T.; Millam, J. *GaussView*, Version 5; Semichem Inc.: Shawnee Mission, KS, 2009.

(43) Tomasi, J.; Mennucci, B.; Cammi, R. *Chem. Rev.* **2005**, *105*, 2999–3093.

(44) Weakliem, H. A.; Hoard, J. L. *J. Am. Chem. Soc.* **1959**, *81*, 549–555.

(45) Shannon, R. D. *Acta Crystallogr.* **1976**, *A32*, 751–767.

(46) Stiefel, E. I.; Brown, G. F. *Inorg. Chem.* **1972**, *11*, 434–436.

(47) Meier, R. Habilitation Thesis, University of Leipzig, Leipzig, Germany, 2003.

(48) Dunitz, J. D. *Tetrahedron* **1972**, *28*, 5459–5467.

(49) McGarvey, B. R. *Inorg. Chem.* **1995**, *34*, 6000–6007.

(50) Evilia, R. F. *Inorg. Chem.* **1985**, *24*, 2076–2080.

(51) (a) Beattie, J. K.; Golligly, J. R.; Hawkins, C. J. *Inorg. Chem.* **1971**, *10*, 317–332. (b) Beattie, J. K. *Acc. Chem. Res.* **1971**, *4*, 253–259.

(52) Oguni, M.; Yoshida, T. M.; Wada, K.; Fukuda, Y.; Ogino, N.; Ito, T.; Miyamae, H.; Sato, K. *J. Phys. Chem. Solids* **2001**, *62*, 613–618.

(53) Jung, W.-S.; Chung, Y. K.; Shin, D. M.; Kim, S.-D. *Bull. Chem. Soc. Jpn.* **2002**, *75*, 1263–1267.

(54) Peters, J. A.; Huskens, J.; Raber, D. J. *Prog. NMR Spectrosc.* **1996**, *28*, 283–350.

(55) (a) Panda, M.; Phuan, P.-W.; Kozlowski, M. C. *Chem. Commun.* **2002**, 1552–1553. (b) Vaiana, L.; Regueiro-Figueroa, M.; Mato-Iglesias, M.; Platas-Iglesias, C.; Esteban-Gomez, D.; de Blas, A.; Rodriguez-Blas, T. *Inorg. Chem.* **2007**, *46*, 8271–8282.

(56) Maigut, J.; Meier, R.; Zahl, A.; van Eldik, R. *Inorg. Chem.* **2008**, *47*, 5702–5719.

(57) (a) Rolla, G. A.; Platas-Iglesias, C.; Botta, M.; Tei, L.; Helm, L. *Inorg. Chem.* **2013**, *52*, 3268–3279. (b) Patinec, V.; Rolla, G. A.; Botta, M.; Tripier, R.; Esteban-Gómez, D.; Platas-Iglesias, C. *Inorg. Chem.* **2013**, *52*, 11173–11184. (c) Esteban-Gomez, D.; de Blas, A.; Rodriguez-Blas, T.; Helm, L.; Platas-Iglesias, C. *ChemPhysChem* **2012**, *13*, 3640–3650. (d) Esteban-Gómez, D.; Cassino, C.; Botta, M.; Platas-Iglesias, C. *RSC Adv.* **2014**, *4*, 7094–7103.

(58) Rodríguez-Rodríguez, A.; Esteban-Gomez, D.; de Blas, A.; Rodríguez-Blas, T.; Botta, M.; Tripier, R.; Platas-Iglesias, C. *Inorg. Chem.* **2012**, *51*, 13419–13429.

(59) Lisowski, J.; Sessler, J. L.; Mody, T. D. *Inorg. Chem.* **1995**, *34*, 4336–4342.

(60) Led, J. J.; Grant, D. M. *J. Am. Chem. Soc.* **1977**, *99*, 5845–5858.

(61) The agreement factor  $AF_i$  is defined as  $AF_i = [\sum(\delta_{iNi}^{exp} - \delta_{iNi}^{calcd})^2 / \sum(\delta_{iNi}^{exp})^2]^{0.5}$ , where  $\delta_{iNi}^{exp}$  and  $\delta_{iNi}^{calcd}$  represent the

experimental and calculated values, respectively. Davis, R. E.; Willcott, M. R. *J. Am. Chem. Soc.* **1972**, *94*, 1744–1745.

(62) Loridant, S.; Digne, M.; Daniel, M.; Huard, T. *J. Raman Spectrosc.* **2007**, *38*, 44–52.

(63) (a) Meier, R.; Boddin, M.; Mitzenheim, S.; Kanamori, K. In *Vanadium and Its Role in Life*; Sigel, H., Sigel, A., Eds.; M. Dekker: New York, 1995; Vol. 31 (Metal Ions in Biological Systems), Chapter 2, pp 45–88. (b) Meier, R.; Boddin, M.; Mitzenheim, S. In *Bioinorganic Chemistry: Transitions Metals in Biology and their Coordination Chemistry*; VCH: Weinheim, 1997; Chapter A-7, pp 69–97. (c) Brausam, A.; Maigut, J.; Meier, R.; Szilagy, P. A.; Buschmann, H.-J.; Massa, W.; Homonnay, Z.; van Eldik, R. *Inorg. Chem.* **2009**, *48*, 7864–7884.

(64) (a) Gampp, H.; Maeder, M.; Meyer, C. J.; Zuberbuehler, A. D. *Talanta* **1985**, *32*, 1133–1139. (b) Gampp, H.; Maeder, M.; Meyer, C. J.; Zuberbuehler, A. D. *Talanta* **1985**, *32*, 95–101. (c) Gampp, H.; Maeder, M.; Meyer, C. J.; Zuberbuehler, A. D. *Talanta* **1986**, *33*, 943–951. (d) Gampp, H.; Maeder, M.; Meyer, C. J.; Zuberbuehler, A. D. *Talanta* **1985**, *32*, 251–264.

(65) L'Epplattienier, F.; Anderegg, G. *Helv. Chim. Acta* **1964**, *47*, 1792–1800.

(66) Higginson, W. C. E.; Samuel, B. *J. Chem. Soc. A* **1970**, 1579–1586.

(67) *NIST Standard Reference Database 46, NIST Critical Stability Constants and Related Thermodynamic Constants of Metal Complexes*, version 7.0; National Institute of Standards and Technology: Gaithersburg, MD, 2003.

(68) Olatunde, A. O.; Dorazio, S. J.; Sperryak, J. A.; Morrow, J. A. *J. Am. Chem. Soc.* **2012**, *134*, 18503–18505.